Published April 21, 2014

to reflect a shift in the steady-state distribution from a more prominent vesicular to a more pronounced plasma membrane localization after overexpression (Han et al., 2004; Atiya-Nasagi et al., 2005).

BARP binds and localizes the different $Ca_v\beta$ subunit isoforms to the plasma membrane

Coimmunoprecipitation experiments using BARP and the different $Ca_v\beta$ subunit isoforms overexpressed in COS-1 cells established that BARP binds to all the different $Ca_v\beta$ isoforms (Fig. 3 A). These associations were corroborated in intact cells using immunofluorescence experiments. When overexpressed in PC12 (Fig. 3 B) or COS-1 (Fig. S2 E) cells, the $Ca_v\beta$ subunits showed, with the exception of $Ca_v\beta2a$, a cytosolic distribution with some degree of nuclear labeling for $Ca_v\beta3$ and $Ca_v\beta4a$ (Dolphin, 2003). Remarkably, overexpression of BARP localized the cytosolic $Ca_v\beta$ isoforms to the plasma membrane. This confirms that the two proteins interact in a cellular context and shows that BARP can influence the subcellular distribution of $Ca_v\beta$ subunits in the absence of $Ca_v\alpha1$. The colocalization index, which in this context reflects the efficiency of recruitment of the different $Ca_v\beta$ subunits by BARP, did not drastically differ, indicating a similar effect of BARP for all isoforms. As a control, BARP M1A/M7A, which utilizes M80 for initiation of translation (Fig. S1 D) and thus lacks the first 79 aa and hence the transmembrane domain, failed to localize $Ca_v\beta3$ to the plasma membrane (Figs. 3 B, a; and S2 E).

When BARP was constitutively and stably overexpressed from a cytomegalovirus promoter in PC12 Tet-On cells (BARP10; Fig. 3 C, a), the localization of endogenous BARP changed from a vesicular pattern in parental cells to a prominent peripheral staining in BARP-overexpressing cells (Fig. 3 C, b). Concomitantly, endogenous $Ca_v\beta1$ and $Ca_v\beta3$, which poorly colocalized with endogenous BARP in untransfected cells, redistributed to the cell periphery upon BARP overexpression (Fig. 3 C, b).

BARP encodes two distinct $Ca_v\beta$-binding domains

To obtain additional insight into the mechanism by which BARP associates with VGCCs, the domains in BARP required for its interaction with the $Ca_v\beta$ subunit were identified. Deletion and alanine-scan mutagenesis of BARP combined with yeast two-hybrid screening (Fig. S3, A and B) and GST pull-down experiments (Fig. S3, C and E) narrowed down the interaction with $Ca_v\beta$ subunits to two domains, termed domain I and domain II. Based on in silico molecular dynamics simulations, domain I (aa 422–442; Fig. 4 A, a) is predicted to fold into an α helix (Fig. S3 D). Mutation of L426, W427, or R430 in BARP abolished the interaction of domain I with the $Ca_v\beta$ subunit (Fig. 4 A, b). The AID of the $Ca_v\alpha1$ subunit and mutants carrying substitutions of aa Y467, W470, and I471, known to be important for binding to $Ca_v\beta$ (Richards et al., 2004), served as a control (Fig. 4 A, a and b).

Previous studies, including crystallographic analysis, established that the AID is associated as an α helix with a hydrophobic groove in $Ca_v\beta$, also termed the AID-binding pocket (ABP; Pragnell et al., 1994; Chen et al., 2004; Richards et al., 2004; Van Petegem et al., 2004). To explore whether domain I could also bind to the ABP, mutations in this region of $Ca_v\beta$ were generated, and their effect on the interaction with BARP was tested. Substitutions of several amino acids in the hydrophobic pocket of the $Ca_v\beta$ subunit impaired its association with BARP domain I (Fig. 4 A, c). This was not caused by an effect of the mutations on the folding of $Ca_v\beta$ because, with the exception of M196A, the different $Ca_v\beta$ mutants still bound the AID.

Because a truncated BARP that lacked domain I still interacted with $Ca_v\beta$, analysis of additional BARP mutants (Fig. S3 E) led to the identification of a second binding region, domain II (aa 525–563; Fig. 4 B, a). Amino acid substitutions in domain II revealed two leucine-phenylalanine pairs (L545-F546 and F549-L550) as important for efficient $Ca_v\beta$ binding (Fig. 4 B). Interestingly, the isolated BARP domain II interacted with $Ca_v\beta3$, $Ca_v\beta2a$, $Ca_v\beta2b$, and $Ca_v\beta4a$ but not with $Ca_v\beta1a$, whereas domain I bound all $Ca_v\beta$ subunits tested (Fig. S3 F).

The effect of the amino acids substitutions in domain I (L426A and W427A) and/or domain II (L545A, F546A, F549A, and L550A) on the association with $Ca_v\beta$ was next analyzed in full-length BARP. Simultaneous mutation of both domains abolished the association of the mutated BARP with the $Ca_v\beta$ (Fig. 4 C). Although the interaction between BARP and $Ca_v\beta$ was more sensitive to the disruption of domain I, the presence of one intact domain was sufficient to confer not only detectable binding but also plasma membrane localization of the $Ca_v\beta$ subunits in cells (Figs. 4 D and S3 H). However, the colocalization index suggests that domain II alone mediates a less efficient localization

GST-BARP domain I were lysed, GST fusion (fus.) proteins were precipitated, and the associated $Ca_v\beta3$ was detected by WB. As a control, $Ca_v\beta3$ was coprecipitated with WT or mutated GST-$Ca_v1.2$ AID. Aliquots of cell lysates were analyzed by WB to monitor protein expression. The black line indicates the rearrangement of lanes for presentation purposes. (c) Identification of amino acids in $Ca_v\beta3$ important for binding to BARP domain I. COS-1 cells expressing GST-BARP domain I or GST-AID with mutated Flag-$Ca_v\beta3$ were lysed, GST fusion proteins were precipitated, and associated $Ca_v\beta3$ was detected by WB. Aliquots of cell lysates were analyzed by WB to monitor protein expression, using two separate gels, as shown. PPT, precipitation. (B) Identification of BARP domain II as a second $Ca_v\beta$ subunit binding region. (a) Amino acid sequence of domain II with residues crucial for the association with $Ca_v\beta$ (red). (b) Identification of amino acids in domain II important for $Ca_v\beta$ binding. COS-1 cells expressing Flag-$Ca_v\beta3$ and WT or mutated GST-BARP domain II were lysed, GST-BARP domain II was precipitated, and the associated Flag-$Ca_v\beta3$ was detected by WB. Aliquots of cell lysates were analyzed by WB to monitor protein expression. (C) Role of domains I and II in the context of full-length BARP in $Ca_v\beta$ binding. COS-1 cells expressing WT BARP or the BARP domain I and/or domain II mutants and Flag-$Ca_v\beta3$ were lysed, Flag-$Ca_v\beta3$ was immunoprecipitated (IP), and the associated BARP was revealed by WB (Ab 72). In a reciprocal experiment, BARP was immunoprecipitated, and bound Flag-$Ca_v\beta3$ was detected. Aliquots of cell lysates were analyzed by WB to monitor protein expression. (D) Roles of domains I and II in the context of full-length BARP in $Ca_v\beta3$ membrane recruitment. PC12 cells expressing Flag-$Ca_v\beta3$ and either BARP WT or mutants affecting domain I and/or domain II were labeled with Ab to Flag (green) and BARP (Ab 72) and processed for immunofluorescence microscopy. Colocalization index is shown in the rightmost images. The dotted lines delimit the cloud shape of the colocalization index. (d–f) Mutation of both domains I and II (db) in BARP abolishes the localization of $Ca_v\beta3$ to the plasma membrane.

Published April 21, 2014

of $Ca_v\beta3$ to the plasma membrane (0.68 ± 0.05) compared with WT BARP (0.80 ± 0.02) or BARP with domain II mutated (0.80 ± 0.02, $P < 0.05$).

BARP modulates the interaction between the $Ca_v\beta$ and $Ca_v\alpha1$ subunits

Because BARP domain I binds to the ABP in $Ca_v\beta$, BARP may interfere with the interaction between $Ca_v\beta$ and $Ca_v\alpha1$. To test this hypothesis, we monitored the stability of a preassembled complex between the $Ca_v\beta_3$ and a GST-AID fusion protein after addition of competitive peptides coding for domain I or, as a control, the AID. Indeed, $Ca_v\beta3$ was displaced by soluble domain I or AID peptides from the immobilized GST-AID and recovered in the supernatant (Fig. 5 A), consistent with BARP domain I and the AID binding in a mutually exclusive manner to the same or an overlapping site in $Ca_v\beta$. Slightly higher concentrations of domain I peptide than AID peptide were required for disruption of the complex.

The biochemical results were corroborated in a cellular context by coexpressing BARP, $Ca_v\beta3$, and $Ca_v\alpha1$ and monitoring their associations in coprecipitation experiments. In the presence of WT BARP, the $Ca_v\beta3$ and $Ca_v\alpha1$ subunits no longer associated (Fig. 5 B). In contrast, coprecipitation was not affected in the presence of BARP with both domain I and II mutated. Mutation of either domain individually partially interfered with the association between the $Ca_v\beta3$ and $Ca_v\alpha1$, showing the importance of domain I and II. Interestingly, mutation of domain I alone allowed the detection of a ternary complex containing BARP, $Ca_v\alpha1$, and $Ca_v\beta3$ (Fig. 5 B, lane 3). As a control, neither $Ca_v\beta3$ nor BARP associated with a mutated $Ca_v\alpha1$ subunit unable to bind $Ca_v\beta3$ (Fig. S4 A), suggesting that BARP does not bind to $Ca_v\alpha1$ directly. Similar results were also obtained for $Ca_v\beta3$ in combination with other $\alpha1$ subunit subtypes (e.g., $Ca_v2.1$ and $Ca_v2.2$; Fig. S4, B and C) and for other $Ca_v\beta$ subunit isoforms (e.g., $Ca_v\beta1a$, $Ca_v\beta2a$, $Ca_v\beta2b$, and $Ca_v\beta4a$; Fig. S4 D).

Coimmunoprecipitation experiments from PC12 cells and the brain confirmed that also endogenous BARP and $Ca_v\beta3$ associate with each other (Fig. 5 C). Interestingly, comparison of the amount of endogenous $Ca_v\beta3$ that was bound to either endogenous or overexpressed BARP in PC12 cells suggested the presence of a significant pool of $Ca_v\beta3$ that is not associated with endogenous BARP. In addition to $Ca_v\beta3$, BARP associated with $Ca_v\beta4$ in cerebellum and cerebrum and to a lesser extent with $Ca_v\beta1$ in the latter (Figs. 5 D and S4 E).

BARP inhibits VGCC activity without affecting cell surface expression of VGCCs

$Ca_v\beta$ subunits modulate Ca^{2+} channel activity by increasing channel current density at the plasma membrane and/or facilitating the trafficking of newly synthesized $Ca_v\alpha1$ subunits from the ER to the plasma membrane (Chien et al., 1995; Dolphin, 2003). To explore the functional role of BARP in regulating VGCC activity, BHK cells stably expressing $Ca_v\alpha1$ ($Ca_v2.1$ or $Ca_v2.2$), $Ca_v\beta1a$, and $Ca_v\alpha2\delta$ subunits to reconstitute P/Q- or N-type VGCCs (Niidome et al., 1994) were transfected with or without WT or mutated BARP cDNAs (Fig. 6, A and B) and subjected to electrophysiological analysis. Compared with controls, in cells overexpressing WT BARP, but not BARP with domains I and II mutated, a drastic reduction in P/Q- or N-type channel Ca^{2+} currents was recorded (Figs. 6, A and B, a and c; and S5 A). Mutation of domain I or II individually resulted in a partial reduction of Ca^{2+} channel activity (Figs. 6, A and B, b and c; and S5 A). Inactivation kinetics in the presence or absence of WT BARP did not significantly differ (P/Q-type channel: control = 78 ± 12 ms, $n = 20$ [Kameyama et al., 1999]; WT BARP = 80 ± 23 ms, $n = 17$).

To analyze whether a defect in Ca^{2+} channel surface expression in the presence of BARP accounts for its inhibitory effect on Ca^{2+} currents, we monitored $Ca_v1.2$ trafficking in tsA201 cells. Similar to BHK cells expressing N or P/Q Ca^{2+} channel subtypes (Fig. 6, A and B), BARP inhibited Ca^{2+} channel activity in tsA201 cells coexpressing $Ca_v1.2$ and $Ca_v\beta3$ (Fig. 6 C). This inhibition was abrogated if both domains I and II were mutated and partially reduced if domain I or II was mutated independently.

Detection of $Ca_v1.2$ on the surface of nonpermeabilized intact tsA201 cells (Altier et al., 2002; Béguin et al., 2006) required coexpression with one of the $Ca_v\beta$ subunits (Figs. 6 D, a; and S5 B), and accordingly, mutation of the AID abolished Ca^{2+} channel cell surface transport (Fig. 6 D, a). Coexpression of $Ca_v1.2$ subunits with BARP, either in the absence or presence of $Ca_v\beta3$, did not significantly affect Ca^{2+} channel surface expression (Fig. 6 D, a). Relative cell surface expression of $Ca_v1.2$ in the presence or absence of $Ca_v\beta3$ and/or BARP was corroborated and quantified by coexpressing in tsA201 cells a $Ca_v\alpha1$ subunit carrying both a luminal (HA) and a cytosolic (EGFP) tag and measuring relative pixel intensities in intact and permeabilized cells (Fig. 6 D, b and c). Although $Ca_v\beta3$, either in the absence of presence of BARP, significantly increased the fraction of $Ca_v\alpha1$ at the cell surface (0.12 ± 0.02 vs. 0.39 ± 0.03, $P < 0.01$), BARP had no significant influence on $Ca_v1.2$ distribution (Fig. 6 C, c). Thus, BARP does not significantly interfere with the role of $Ca_v\beta$ in facilitating cell surface expression of Ca^{2+} channels and thus most likely inhibits channel activity at the plasma membrane.

BARP negatively modulates VGCC activity and Ca^{2+}-regulated secretion

To elucidate the role of BARP in physiological processes linked to VGCC function, we explored the effects of BARP on VGCC activity and Ca^{2+}-dependent hormone secretion in PC12 cells (Béguin et al., 2001). First, we took advantage of the observation that endogenous BARP expression varies in different PC12 clones and is higher in ATCC PC12 cells (CRL-1721) than in PC12 Tet-On cells (Takara Bio Inc.; Fig. 7 A, a). Correlating with the different BARP expression levels in these cells, endogenous Ca^{2+} channel current densities were lower in ATCC PC12 cells and significantly inhibited in PC12 Tet-On cells stably expressing BARP (Fig. 7 A, b). These results were corroborated in PC12 cells transiently expressing BARP. An almost complete reduction of endogenous Ca^{2+} currents was recorded in cells overexpressing WT BARP, whereas BARP with both domains I and II mutated had no significant effect on VGCC activity (Fig. 7 B).

Importantly, inhibition of VGCC activity by BARP had an effect on Ca^{2+}-triggered exocytosis (Fig. 7 C). Correlating with

Published April 21, 2014

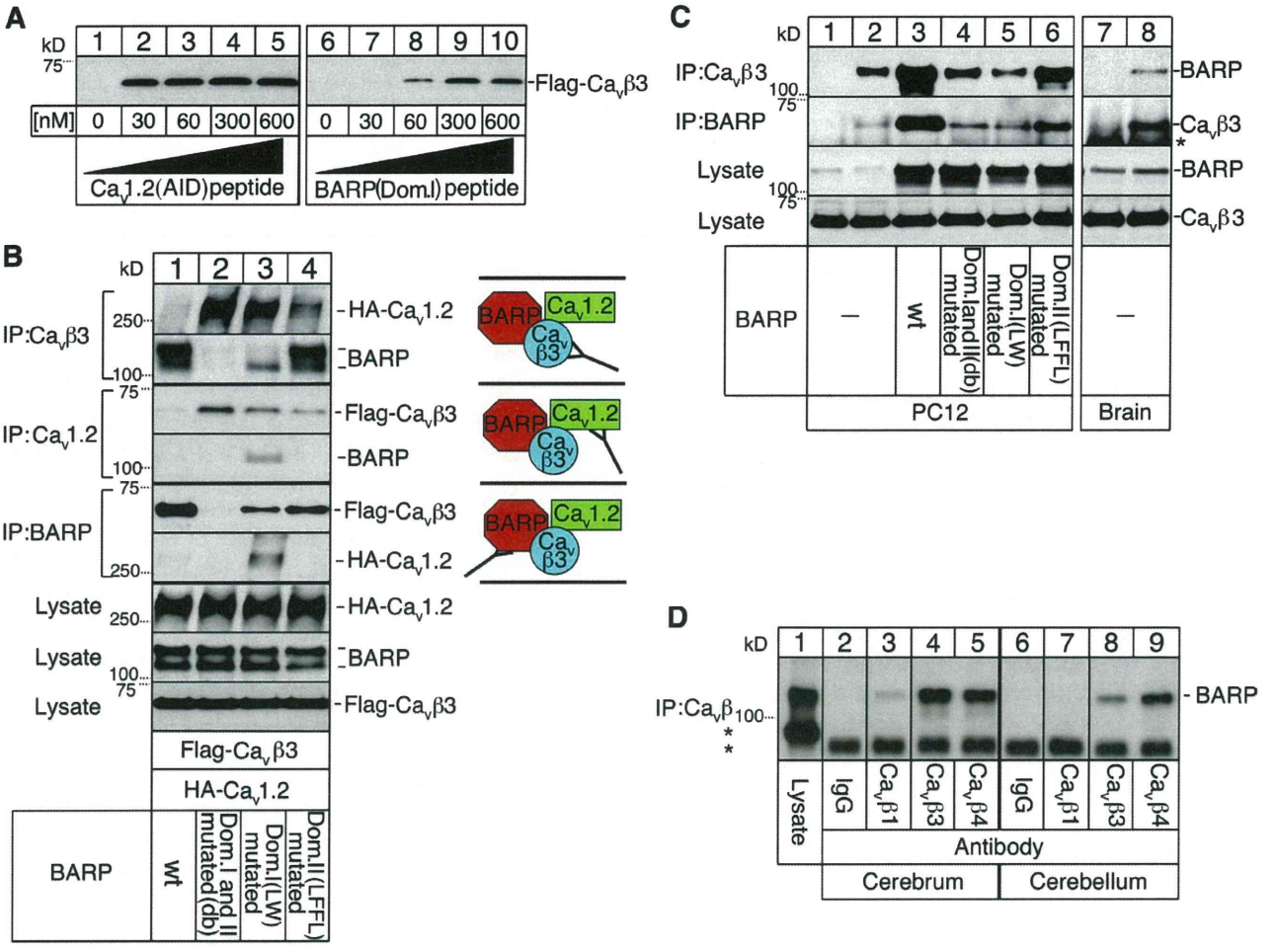

Figure 5. **Competition between the AID of $Ca_v\alpha1$ and BARP domain I for $Ca_v\beta$ binding and association of endogenous BARP and $Ca_v\beta$.** (A) BARP domain I (Dom.I) peptides dissociate a preformed AID–$Ca_v\beta3$ complex. Flag-$Ca_v\beta3$ expressed in COS-1 cells was isolated using a GST-AID fusion protein. The complex was incubated with increasing amounts of AID or BARP domain I peptide as indicated. Flag-$Ca_v\beta3$ displaced from the immobilized GST-AID was recovered in the supernatant and detected by WB using two separate gels, as shown. No Flag-$Ca_v\beta3$ was detected in the supernatant in the absence of peptides, showing that the immobilized $Ca_v\beta3$–AID complex did not dissociate over the duration of the experiment. (B) BARP overexpression interferes with the association between $Ca_v\beta$ and $Ca_v1.2$ subunits. COS-1 cells were cotransfected with cDNAs for WT or mutated BARP together with Flag-$Ca_v\beta3$ and HA-$Ca_v1.2$ subunits. Flag-$Ca_v\beta3$, HA-$Ca_v1.2$, or BARP was immunoprecipitated (IP), and the associated Ca^{2+} channel subunits or BARP was revealed by WB. Aliquots of cell lysates were analyzed by WB to monitor protein expression. db, both domains I and II mutated. (C) Association of endogenous BARP with $Ca_v\beta3$ in PC12 cells and brain. Endogenous $Ca_v\beta3$ was immunoprecipitated from PC12 cells or brain lysates, and the associated endogenous BARP was revealed by WB (mAb 12B1). In a reciprocal experiment, BARP was first immunoprecipitated (mAb 8B2), and bound $Ca_v\beta3$ was detected. Control IgG did not pull down BARP or $Ca_v\beta3$ (lanes 1 and 7). Aliquots of the cell lysates were analyzed by WB using two separate gels, as shown, to monitor the expression of endogenous or overexpressed proteins. The asterisk shows the band for IgG heavy chain. (D) Association of endogenous BARP with $Ca_v\beta1$, $Ca_v\beta3$, and $Ca_v\beta4$ in the cerebrum and cerebellum. Endogenous $Ca_v\beta$ subunits were immunoprecipitated from lysates, and the associated endogenous BARP was revealed by WB (mAb 12B1). Control IgG did not pull down BARP (lanes 2 and 6). Aliquots of the cell lysates were analyzed by WB to monitor BARP expression. Black lines indicate the rearrangement of lanes for presentation purposes. In addition, note that lane 1 represents a shorter exposure of the same membrane than the other lanes. The asterisks show the band for IgG heavy chain and a nonspecific band that did not coprecipitate with $Ca_v\beta$.

the Ca^{2+} channel recordings, overexpression of BARP strongly inhibited Ca^{2+}-dependent growth hormone secretion. Mutation of either domain I or II individually led to intermediate effects, whereas BARP carrying mutations in both $Ca_v\beta$ subunit binding sites only marginally affected growth hormone secretion.

Relative cell surface expression of $Ca_v1.2$ in the presence or absence of $Ca_v\beta3$ and/or BARP was also analyzed in PC12 cells as described for tsA201 cells (Fig. 6 D, b and c). Although $Ca_v\beta3$, either in the absence or presence of BARP, significantly increased the fraction of $Ca_v\alpha1$ at the cell surface (0.22 ± 0.01 vs. 0.45 ± 0.01, $P < 0.01$), BARP had no significant influence on $Ca_v1.2$ channel distribution in PC12 cells (Fig. 7 D). Collectively, these data establish BARP as a negative regulator of Ca^{2+}-dependent exocytosis, most likely by modulating VGCC activity at the plasma membrane.

Silencing of BARP enhances VGCC activity and Ca^{2+}-evoked secretion

We next analyzed the effect of silencing BARP in ATCC PC12 cells because these express significant levels of the protein endogenously (Fig. 7 A, a). Three shRNAs (A, B, and C) that target different regions of the BARP mRNA (Fig. 8 A, a) were stably transfected into PC12 cells, and two independent clones for each shRNA were selected. Expression levels of BARP in

Published April 21, 2014

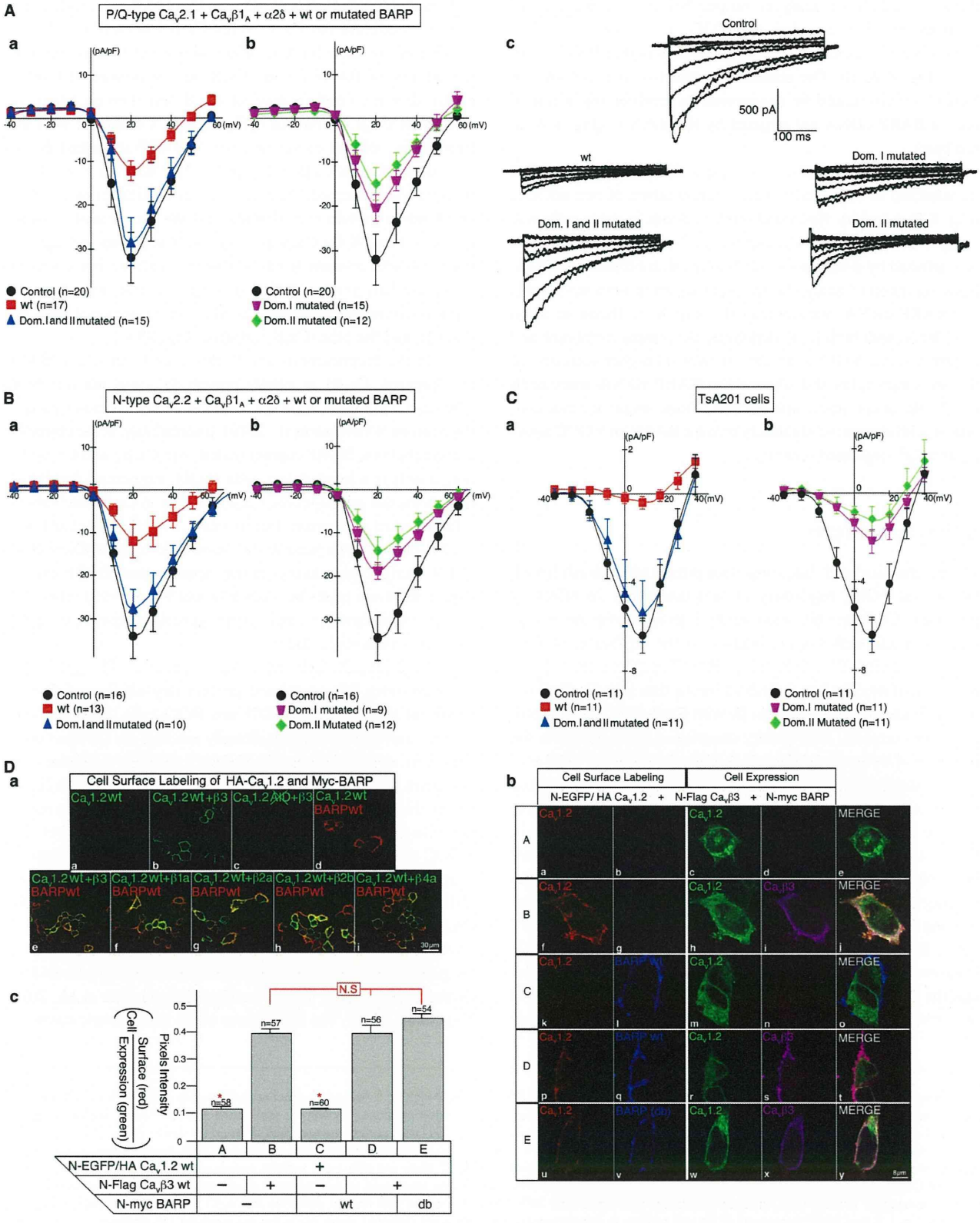

Figure 6. **BARP down-regulates voltage-gated Ca^{2+} channel activity without affecting its cell surface expression.** (A–C) BARP down-regulates VGCC activity. Effect of BARP on activity of P/Q (A)- or N (B)-type Ca^{2+} channels reconstituted in BHK cells or on VGCCs in tsA201 cells (C). (A and B) BHK cells stably expressing Ca$_v$2.1 (P/Q type) or Ca$_v$2.2 (N type) together with Ca$_v\beta$1a and Ca$_v\alpha2\delta$ were transfected with a vector carrying WT or mutated BARP and EGFP cDNAs, and cells expressing EGFP were selected for electrophysiology. (C) tsA201 cells were cotransfected with a vector carrying WT or mutated BARP and mCherry cDNAs, a vector containing Ca$_v$1.2, and an internal ribosomal entry site followed by Ca$_v\beta$3 and EGFP cDNAs, and cells expressing mCherry and EGFP were selected for electrophysiology. Current–voltage (I–V) relationships of the different Ca^{2+} channels in the different cells

Published April 21, 2014

the six PC12 clones analyzed ranged between 10 and 25% of controls (Fig. 8 A, b and c), and VGCC Ca^{2+} current densities in these clones were between 50 and 140% higher than in controls (Fig. 8 A, d). The stimulatory effect of the shRNAs on VGCC activity could be suppressed by transfecting a rescue mouse BARP cDNA not targeted by the shRNAs (Fig. 8 A, d, red bars).

Endogenous BARP expression was also silenced by transient transfection of PC12 cells with a combination of two siRNAs (Fig. 8 B, a and b). Neurotransmitter release in these cells was analyzed to determine whether the Ca^{2+}-evoked secretion was also affected by silencing BARP. No significant differences in the basal secretion of acetylcholine were apparent between control and BARP siRNA–transfected cells (Fig. 8, c). However, upon stimulation with high K^+ to depolarize the plasma membrane and in turn activate VGCCs, an almost twofold higher secretion of the neurotransmitter was observed in BARP siRNA–transfected PC12 cells as compared with controls. These results are thus consistent with a negative regulatory role for BARP on VGCC activity and Ca^{2+}-regulated secretion.

Discussion

The biochemical and functional data presented establish BARP as a novel VGCC regulatory protein that exerts its effect by binding to $Ca_v\beta$ subunits and thereby interferes with the association of $Ca_v\beta$ with $Ca_v\alpha1$, leading to the inhibition of Ca^{2+} channel activity. Two domains in BARP associate with $Ca_v\beta$. Mutation of domain I to abolish its interaction with $Ca_v\beta$ allows BARP to associate, via domain II, with $Ca_v\beta$ and $Ca_v\alpha1$ to form a ternary complex. This ternary complex is not detected in the presence of a functional domain I, likely because domain I prevents a stable association between $Ca_v\alpha1$ and $Ca_v\beta$, and could thus in vivo be short lived or transient. Domain I is predicted to acquire an α-helical structure that interacts with the ABP in $Ca_v\beta$. In vitro, the binding between domain I and the ABP occurs in the nanomolar range and is of lower apparent affinity than the binding of the AID to $Ca_v\beta$, which ranges from 2 to 54 nM, depending on the particular $Ca_v\alpha1$ and $Ca_v\beta$ species (De Waard et al., 1995; Bell et al., 2001; Cantí et al., 2001; Geib et al., 2002; Opatowsky et al., 2003). In cells, however, evidence suggests that the $Ca_v\alpha1$ and $Ca_v\beta$ interaction has a lower affinity and is reversible (Hidalgo et al., 2006; Buraei and Yang, 2010). A local concentration of BARP (e.g., domain I) could thus be sufficiently high to modulate the $Ca_v\alpha1$ AID–$Ca_v\beta$ interaction. Alternatively, a cooperative binding of domains I and II could increase the affinity of BARP for the $Ca_v\beta$, and/or domain II binding could alter the conformation of $Ca_v\beta$ and thereby lower the affinity of $Ca_v\beta$ for the AID (Fig. S5 D). Consistent with this hypothesis, cellular overexpression of BARP abolished the association between $Ca_v\beta$ and $Ca_v\alpha1$ only if domain II–mediated binding was preserved. Posttranslational modifications of BARP or a binding protein may also regulate the cooperation between domains I and II for $Ca_v\beta$ association. The region in $Ca_v\beta$ that interacts with domain II has not been identified but could involve the SH_3 and/or HOOK domain because they show the highest divergence between $Ca_v\beta1a$, which does not bind domain II, and the other $Ca_v\beta$ isoforms (Fig. S3 G).

In the hippocampus and Purkinje cells, in which BARP is expressed, $Ca_v\beta1$ is mostly present in soma and dendrites, whereas $Ca_v\beta3$ and $Ca_v\beta4$ are found in axons and other parts of the neurons (Obermair et al., 2010). Interestingly, in the cerebrum and cerebellum, BARP coprecipitated with $Ca_v\beta3$ and $Ca_v\beta4$ but not, or only to a lesser extent, with $Ca_v\beta1$, suggesting that BARP may associate with specific $Ca_v\beta$ subunits in particular subcellular domains of neurons. For instance, BARP colocalized with BDNF, indicating its presence on dense core vesicles (Dieni et al., 2012). Intriguingly, during mouse development, BARP expression in the brain peaks between E18 and P7, a period crucial for neural circuit formation and synaptogenesis (Ullian et al., 2004; Christopherson et al., 2005).

$Ca_v\beta$ subunits facilitate surface expression of L-type VGCC by preventing ER-associated protein degradation of Cav1.2 (Altier et al., 2011). In tsA201 and PC12 cells, BARP inhibits VGCC activity without significantly altering the distribution of the $Ca_v\alpha1$ subunit between the cell surface and intracellular compartments and is thus unlikely affecting ER exit and stability of $Ca_v\alpha1$. However, it is well documented that $Ca_v\beta$ plays an important role in modulating, mainly via the IS6-AID linker, not only VGCC trafficking but also gating, including voltage-dependent activation, inactivation, and facilitation kinetics (Buraei and Yang, 2010). For instance, RGK GTPases, through association with $Ca_v\beta$ and/or $Ca_v\alpha1$, not only regulate cell surface expression of VGCCs but also directly modulate currents of the channel at the plasma membrane by lowering channel opening probabilities and/or immobilizing VGCC voltage sensors (Fan et al., 2010; Yang et al., 2010). The time course of the macroscopic current in

expressing the different BARP proteins (a and b) as well as the traces for P/Q (c)- and N (Fig. S5 A)-type channel recordings are shown. Three independent experiments were performed each, and the data were combined to obtain the indicated *n* values. Shown are the means ± SEM. Paired Student's *t* test at 20 mV. For P/Q-type channels, control versus BARP WT or domain II mutated ($P < 0.01$) and control versus BARP domain I mutated ($P < 0.05$) are shown. For VGCCs in tsA201 cells, control versus BARP WT and domains I or II mutated ($P < 0.01$) are shown. For better readability, the data are plotted in two individual graphs; hence, the curve for the controls in a and b is identical. (D) BARP does not affect cell surface expression of Ca^{2+} channels in tsA201 cells. (a) Cell surface expression of HA epitope–tagged $Ca_v1.2$ and N-Myc–BARP was monitored in the presence or absence of $Ca_v\beta3$ by immunofluorescence microscopy. tsA201 cells were cotransfected with cDNAs for WT HA-$Ca_v1.2$ or an AID mutant defective in $Ca_v\beta3$ binding, Myc-BARP, and $Ca_v\beta$ isoforms. $Ca_v1.2$ and BARP expressed at the cell surface in nonpermeabilized cells were detected using Ab to the extracellular HA epitope in $Ca_v1.2$ and Myc in BARP. (b) Cell surface expression of N-EGFP/HA-$Ca_v1.2$ and N-Myc–BARP was monitored in the presence or absence of $Ca_v\beta3$. tsA201 cells were cotransfected with cDNAs for N-EGFP/HA-$Ca_v1.2$ alone (A) either together with N-Flag–$Ca_v\beta3$ (B) or N-Myc–BARP (C) or with Flag-$Ca_v\beta3$ and WT BARP or BARP with domains I and II mutated (D and E). $Ca_v1.2$ and BARP expressed at the cell surface in nonpermeabilized cells were detected using Ab to the extracellular HA epitope in $Ca_v1.2$ and Myc in BARP. Cellular expressions of EGFP-$Ca_v1.2$ and $Ca_v\beta3$ are shown. Merged images are shown on the right. (c) Quantification of channel cell surface expression is stated as the relative surface expression of HA versus EGFP-$Ca_v1.2$ (red/green). Unpaired Student's *t* test: *, $P < 0.01$. db, both domains I and II mutated; Dom., domain.

Published April 21, 2014

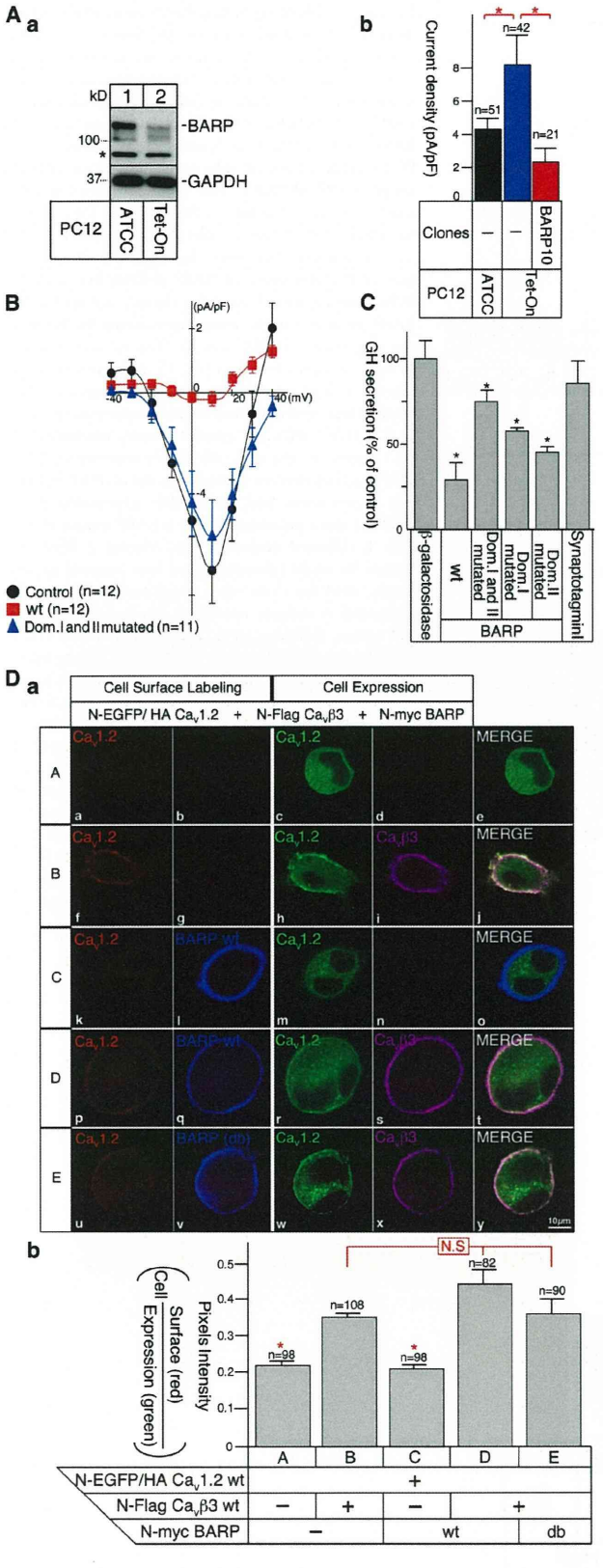

Figure 7. **BARP down-regulates VGCC activity at the plasma membrane and inhibits Ca^{2+}-dependent hormone secretion in PC12 cells.** (A) Expression of endogenous BARP in different PC12 cell lines and VGCC Ca^{+} current recordings in ATCC PC12 cells, PC12 Tet-On cells, and PC12 Tet-On cells stably overexpressing BARP (BARP10). (a) WB analysis. BARP detected in lysates from PC12 cells (ATCC) and PC12 Tet-On cells using mAb 12B1. GAPDH served as a control. The asterisk indicates the nonspecific band detected in PC12 cells. (b) Ca^{+} current recordings. Seven independent experiments were performed for each cell line, and the data were combined each to obtain the indicated *n* values. Shown are the means ± SEM for the indicated *n* values. Paired Student's *t* test. *, $P < 0.05$. (B) BARP down-regulates endogenous Ca^{2+} channel activity in PC12 cells. PC12 cells were transfected with a vector carrying WT or mutated BARP and EGFP cDNAs. Cells expressing EGFP were selected for electrophysiology. I–V relationships of Ca^{2+} channels for cells expressing the different BARP proteins are shown. Three independent experiments were performed, and the data were combined to obtain the indicated *n* values. Shown are the means ± SEM. Paired Student's *t* test at 20 mV: control versus BARP WT or domains I and II mutated ($P < 0.01$). (C) BARP inhibits Ca^{2+}-triggered growth hormone secretion in PC12 cells. PC12 cells were cotransfected with cDNAs for hGH and either β-galactosidase, synaptotagmin I, or WT or mutated BARP. hGH secretion in response to high K^{+} stimulation from cells coexpressing hGH and β-galactosidase was used as a control (100%). Shown are the means ± SEM; $n = 4$ independent experiments; unpaired Students *t* test: *, $P < 0.05$. (D) BARP does not affect cell surface expression of Ca^{2+} channels in PC12 cells. (a) Cell surface expression of N-EGFP/HA-$Ca_v1.2$ and N-Myc–BARP monitored in the presence or absence of $Ca_vβ3$ by immunofluorescence microscopy. PC12 cells were electroporated with cDNAs for N-EGFP/HA-$Ca_v1.2$ alone (A) either together with N-Flag–$Ca_vβ3$ (B) or N-Myc–BARP (C) or with Flag-$Ca_vβ3$ and WT BARP or BARP with mutated domains I and II (D and E). $Ca_v1.2$ and BARP expressed at the cell surface in nonpermeabilized cells were detected using Ab to the extracellular HA epitope in $Ca_v1.2$ and Myc in BARP. Cellular expression of EGFP-$Ca_v1.2$ and $Ca_vβ3$ are shown. Merged images are shown on the right. (b) Quantification of channel cell surface expression is expressed as the relative surface expression of HA versus EGFP-$Ca_v1.2$ (red/green). Shown are the means ± SEM. Unpaired Student's *t* test: *, $P < 0.01$. db, both domains I and II mutated; Dom., domain.

the presence of BARP was not modified, suggesting that single channel conductance, opening probability, or sensor movement rather than the kinetic or activation threshold is affected. More detailed electrophysiological studies of single channel dynamics will be required to elucidate how BARP affects VGCC activity. Although BARP does not alter surface expression of the $Ca_vα1$ subunit in tsA201 and PC12 cells, we cannot rule out an effect on VGCC trafficking in other cell types and/or under certain conditions.

One possible function of BARP could be that of an acceptor/donor for the reversible transfer of $Ca_vβ$ from/to the $Ca_vα1$ subunit. Such a reversible transfer could provide an attractive mechanism to retain the $Ca_vβ$ in the active zone to allow for the rapid modulation of VGCC activity. Thus, BARP may provide the first example of a negative modulation though the displacement of $Ca_vβ$ from the $Ca_vα1$ subunit. The presynaptic protein Rim1 also interacts with $Ca_vβ$ to anchor it to secretory vesicles (Kiyonaka et al., 2007; Gandini et al., 2011; Weiss et al., 2011), but in contrast to BARP, Rim1 stimulates Ca^{2+}-dependent secretion by preventing voltage-dependent VGCC inactivation (Kiyonaka et al., 2007).

BARP is abundant in the brain and pancreas, in which Ca^{2+}-regulated exocytosis through activation of L-type VGCC plays important roles in the release of neurotransmitters and hormones. Calcium channelopathies are congenital or noninherited muscular, neurological, and cardiac diseases associated with the gain or loss of VGCC function (Bidaud et al., 2006). Ca^{2+} channel inhibitors represent one of the most active areas of pharmacological drug development. Overexpression of BARP, or peptides encoding domains I and/or II, may be used as

Published April 21, 2014

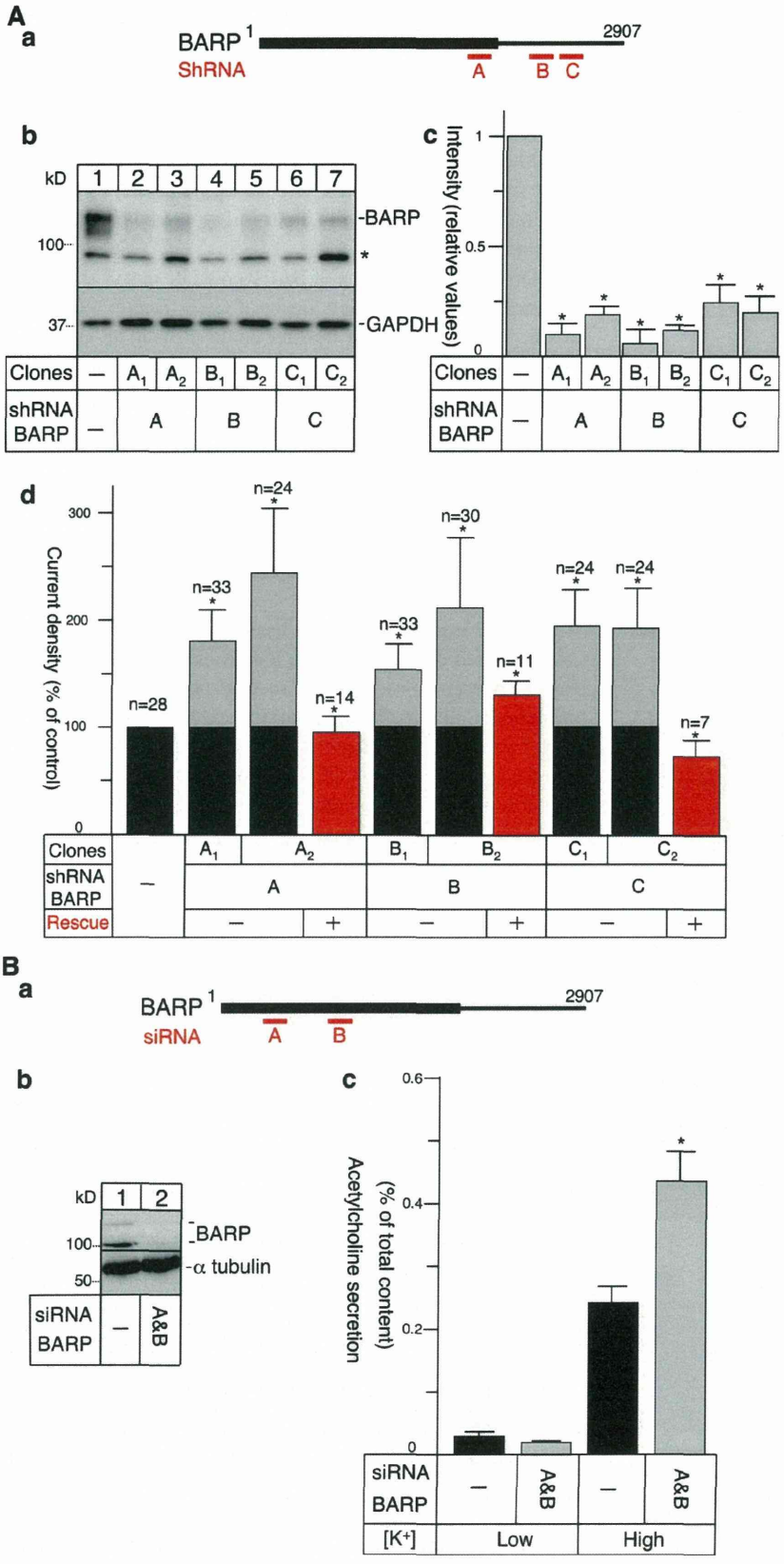

Figure 8. **Silencing of BARP enhances VGCC activity and Ca^{2+}-evoked secretion.** (A) Silencing of BARP enhances VGCC Ca^{2+} currents. (a) Schematic location of three BARP shRNA target sequences (A–C) in the rat BARP mRNA. (b) Silencing of endogenous BARP by shRNAs. WB detection of endogenous BARP and GAPDH in lysates from either ATCC PC12 control cells or cells constitutively expressing single BARP shRNAs. The asterisk shows a non-specific band detected in PC12 cells. Two clones for each shRNA were selected, and BARP (mAb 12B1) and GAPDH were detected. (c) Quantification of the efficiency of BARP shRNA knockdown. WBs were scanned, and the density values for the BARP protein bands were normalized to those of the respective GAPDH bands. The relative amount of BARP present in control PC12 cells was set to 1. Means ± SEM are shown for $n = 5$; unpaired Student's t test control versus shRNA-expressing clones: *, $P < 0.01$. (d) Ca^{2+} current density recordings in PC12 control cells and cells stably expressing BARP shRNAs. The control current was set to 100. For rescue experiments (red bars), cells expressing BARP shRNAs were transfected with a BARP mouse cDNA with a different codon usage. Means ± SEM are shown for eight (silencing) and four (rescue) experiments, and the data were combined to obtain the indicated n values; unpaired Student's t test control versus shRNA-expressing clones: *, $P < 0.05$. (B) Silencing of BARP enhances Ca^{2+}-evoked secretion. (a) Schematic location of the two BARP siRNA target sequences (A and B) in the rat sequence. (b) Silencing of endogenous BARP by siRNAs. WB detection of endogenous BARP (mAb 12B1) and α-tubulin as a control in lysates from ATCC PC12 cells or cells transfected with both siRNAs. Three independent experiments were performed, and a representative example is shown. (c) Acetylcholine secretion was determined in control and siRNA-transfected PC12 cells after low or high potassium stimulation. Shown are the means ± SEM; $n = 4$ independent experiments; unpaired Student's t test: *, $P < 0.05$.

Published April 21, 2014

Ca^{2+} channel modulators. The identification of BARP may thus open new avenues for the design of novel therapeutic VGCC blockers.

Materials and methods

Molecular biology

The yeast two-hybrid screens were performed as follows. A yeast strain L40 (*MATa trp1 leu2 his3 LYS2::lexA-HIS3 URA3::lexA-lacZ*) was transformed with a derivative of pBTM116 encompassing $Ca_v\beta3$ subunit amino acid residues 50–484 fused to the LexA DNA-binding domain. A mouse MIN6 cell cDNA library was then screened, and after histidine selection, positive clones were further confirmed to be true positives by β-galactosidase activity measurement. Eight positive clones that presented fragments of BARP cDNA were found. A BARP alanine mutagenesis scan for aa 280–485 was assessed by substituting three by three the amino acids of BARP to alanine and processed for β-galactosidase activity measurements using paper filters stained with 5-bromo-4-chloro-3-indolyl-β-D-galactopyranoside (Béguin et al., 2001). Full-length mouse BARP was isolated by conventional screening of MIN6 cDNA libraries with a partial mouse cDNA. Sequence analysis of EST clones from mouse, rat, and human (see legend of Fig. S1 A) confirmed that BARP is translated from a 3-kb transcript. Rat $Ca_v\beta1b$, $Ca_v\beta21$ (e.g., β2A), $Ca_v\beta3$, and $Ca_v1.2$ were originally cloned in S. Seino's laboratory, and the $Ca_v2.1$ and $Ca_v2.2$ cDNAs were a gift from T.W. Soong (National University of Singapore, Singapore) and T.P. Snutch (University of British Columbia, Vancouver, British Columbia, Canada). Mouse $Ca_v\beta4a$ was obtained from the I.M.A.G.E. Consortium (4501980). Epitope-tagged constructs (Flag, HA, Myc, GST, and EGFP) as well as deletion and point mutants were generated by PCR-based methods and subcloned into the pME18S vector containing an SRα promoter. The internally HA-tagged $Ca_v1.2$ has been described elsewhere (Altier et al., 2002; Béguin et al., 2006). In brief, the HA sequence was introduced in the S5-H5 loop in position 697 of rabbit $Ca_v1.2$. The amino acid sequence is defined as MQTRH-HA-MQTR (MQTR are amino acids of $Ca_v1.2$, which were duplicated, underlined is an additional amino acid, and the HA sequence is without the first methionine). Northern blot analysis was performed under standard stringency hybridization and washing conditions using mouse and human BARP cDNA probes.

Ab production

Polyclonal anti-BARP Ab 72 was custom made (BioGenes) by injecting rabbits with a BARP peptide (^{131}NEAALFEQSRK^{141}) conjugated to hemocyanin and affinity purified. A GST-BARP fusion protein (aa G125-A698) was injected into mice to generate mAb 12B1 and 8B2. Epitope mapping using truncated forms of BARP located the epitopes recognized by 8B2 and 12B1 to a region between aa 380 and 698.

Cell culture and transfection

COS-1, standard (CRL-1721), and Tet-On PC12 cells as well as BHK and tsA201 cells were grown and transiently transfected with WT or mutated cDNAs using Lipofectamine (LTX; Invitrogen) and jetPRIME (Polyplus Transfection) for biochemical and immunofluorescence experiments, respectively (Béguin et al., 2001, 2005b, 2006, 2007; Mahalakshmi et al., 2007a,b). A plasmid carrying a hygromycin resistance gene and the BARP cDNA downstream of a cytomegalovirus promoter was transfected into PC12 cells using Lipofectamine LTX. PC12 clones stably overexpressing BARP were selected and maintained in 0.2 µg/µl hygromycin. BHK cells expressing functional Ca^{2+} channels reconstituted by expression of rabbit cDNAs for the different subunits have been characterized (Mori et al., 1991; Fujita et al., 1993). Silencing of BARP in PC12 cells was achieved using the pSUPER RNAi System (Oligoengine) system and shRNAs A (5′-TTCTCAAGTCCATATACGG-3′), B (5′-TAGTGTTGATTGTCCTCCT-3′), and C (5′-CTTTGTAGCAACTGTACCT-3′) with selection and maintenance of stable clones in 400 µg/ml G418. Alternatively, PC12 cells were transiently transfected using DharmaFECT (Thermo Fisher Scientific) with siRNAs A (5′-GGAUUUCCAUCACCUCAAG-3′) and B (5′-CAUGCUGACUUCAUUCAAU-3′) designed by Thermo Fisher Scientific and used for analysis 48 h after transfection. For cell surface expression analysis, PC12 cells were electroporated (1,410 V at 30 ms) using the Neon Transfection System (Invitrogen). Primary hippocampal neurons were purchased from Cambrex and cultured according to the manufacturer's instructions. Cerebellar primary cultures were prepared as previously described (Launey et al., 2004) with substitution of B27 by the N21 supplement (Chen et al., 2008). In brief, cerebella were removed from 19-d Wistar rat fetuses, minced in Ca^{2+}/Mg^{2+}-free Hank's saline (Gibco), and digested with 0.01% trypsin (15 min at 37°C). After trituration, the suspension was plated at 5,000 cells/mm^2 on 18-mm glass coverslip (Thermo Fisher Scientific) coated with poly-L-lysine and poly-L-ornithine. Culture medium (37°C at 5% CO_2) consisted of glutamate/aspartate-free DMEM/F12 supplemented with 10 mg/ml bovine insulin, 100 mg/ml BSA, 1 mg/ml gentamycin, 200 mg/ml glutamine, 100 mg/ml human apotransferrin, 40 nM progesterone, 100 nM putrescine, 30 nM sodium selenite, 500 pg/ml triiodothyronine, 3% heat-inactivated horse serum (Gibco), and 25% of astrocyte-conditioned medium (Sumitomo Corp.), renewed by half twice a week. Cells were used at 3–4 wk. All animal experimentation was approved by the RIKEN or Institute of Molecular and Cell Biology Institutional Animal Care and Use Committees. Cells were maintained in culture for 3–4 wk before immunofluorescence microscopy experiments. Tunicamycin treatment was performed by incubating COS-1 cells immediately after transfection for 2 d with 10 µg/ml tunicamycin (Sigma-Aldrich).

Immunoprecipitation and Western blot (WB) analysis

Cell homogenates were prepared in lysis buffer (50 mM Tris-HCl, pH 7.5, 100 mM NaCl, 1 mM $MgCl_2$, and 0.5% Triton X-100) supplemented with protease inhibitors and used for coimmunoprecipitation and WB analysis as previously described (Béguin et al., 2006). For better resolution of higher molecular weight proteins, some samples were run on Tris-acetate gels (7%) according to the manufacturer's instructions (Invitrogen). Rat mAb to HA (Roche), mouse mAb to Flag (M2; Sigma-Aldrich), $Ca_v\alpha1$ (NeuroMab), GAPDH, MAP2, calbindin (EMD Millipore), synaptotagmin (Stressgen), GST (Santa Cruz Biotechnology, Inc.), $Ca_v\beta3$ (Alomone Labs), GFAP (Sigma-Aldrich), and Ab to BARP (72 and 8B2) were used. Rat cerebrum and cerebellum were manually dissociated and immediately homogenized in the same lysis buffer using 15 strokes of a glass Teflon homogenizer followed by one freeze/thaw cycle. Insoluble material was removed by centrifugation. Brain, skeletal muscle, and heart lysates were purchased from Zyagen Laboratories. At least three independent experiments were performed, and representative examples are shown.

In vitro transcription/translation

BARP was synthesized in vitro using the quick-coupled transcription/translation system (TnT; Promega) according to the manufacturer's protocol.

In vitro peptide competition

For dissociation experiments, AID (^{445}AKARGDFQKLREKQQLEEDLKGALDAATQAED^{476}) and BARP domain I (^{422}SYRDLWSLRASLELHAATASD^{442}) peptides were synthesized (Mimotopes). $Ca_v\beta3$ was pulled down from cell lysates with a GST-AID (aa A445–D476) fusion protein. After extensive washing in lysis buffer (50 mM Tris-HCl, pH 7.5, 100 mM NaCl, 1 mM $MgCl_2$, and 0.5% Triton X-100) supplemented with protease inhibitors to remove unbound $Ca_v\beta3$, increasing concentrations of peptides (30, 60, 300, and 600 nM) were added in lysis buffer. After a 4-h incubation on ice, 10% of the supernatant containing any dissociated $Ca_v\beta3$ was analyzed by SDS-PAGE and WB. In the absence of competitive peptides, the GST-AID–$Ca_v\beta3$ subunit complex remained stable over the 4-h incubation period. At least three independent experiments were performed, and representative examples are shown.

Immunocytochemistry and immunohistochemistry

N-Flag–$Ca_v\beta$ subunits and BARP or N-Myc–BARP overexpressed in PC12 and COS-1 cells were stained with mouse anti-Flag (M2; Sigma-Aldrich) and rabbit anti-BARP Ab 72 or a rabbit Ab to Myc (Sigma-Aldrich) followed by Cy3-labeled donkey anti–rabbit IgG (Jackson ImmunoResearch Laboratories, Inc.) and Alexa Fluor 488 goat anti–mouse IgG (Molecular Probes) secondary Ab as previously described (Béguin et al., 2005b). PC12, primary hippocampal, or cerebellar cells were stained with rabbit Ab to MAP2 (EMD Millipore), calbindin (EMD Millipore), and GFAP (Sigma-Aldrich), BDNF (EMD Millipore), or with mouse mAb to synaptotagmin (Stressgen). Rat brains were mechanically cut into 0.3-µm-thick sections and incubated in 10% TCA for 30 min before staining. Mouse pancreas was fixed in 4% PFA and subjected to standard ethanol/xylene processing, embedded into paraffin, cut into 0.5-µm sections, and rehydrated in graded ethanol. Slices were then washed three times with 30 mM PBS-glycine and incubated 1 h in a blocking buffer (10% goat serum, 2% BSA, and 0.4% Triton X-100), and Ab incubations were performed as described in this paragraph. For the 72 BARP Abs, antigen retrieval was achieved by incubating fixed slices for 30 min in 10 mM Tris-HCl, pH 9.0, 1 mM EDTA, and 0.05% Tween 20 at 80°C followed by three washes in PBS

Published April 21, 2014

before blocking. Antigen retrieval in pancreas sections was performed in citrate buffer (10 mM sodium citrate, pH 6, and 0.05% Tween 20) in an autoclave (Retriever 2100; Prestige Medical). Mouse mAb to glucagon (Abcam) or guinea pig Ab to insulin (Abcam) was used to stain α and β cells, respectively, in pancreatic islets. Labeled specimens were mounted in FluorSave (Vector Laboratories) or ProLong Gold (Invitrogen) and visualized using a confocal microscope (LSM 510 Meta [Carl Zeiss] or FluoView FV1000 [Olympus]). Antigen preabsorption experiments were performed by incubating GST-BARP (G125-A698) fusion protein (1 µg) linked to Sepharose beads with anti-Myc and anti-BARP Ab (72, 12B1, or 8B2) in lysis buffer for 2 h at 4°C. After a short centrifugation, the supernatant was collected and mixed with blocking buffer (1:1) before being applied to PFA-fixed cells expressing N-Myc–BARP or cerebellum slices fixed in 10% TCA.

Cell surface expression assays

To detect cell surface expression of N- or C-terminally tagged BARP or a $Ca_v1.2$ carrying a tag in an extracellular loop (Béguin et al., 2001; Altier et al., 2002), we took advantage of the fact that Abs to the tags when added to nonpermeabilized intact cells only bind and label the cells if the tag is exposed on the cell surface. Thus, intact transfected COS-1, tsA201, or BHK cells were incubated with 2 µg/ml rat anti-HA (Roche) and/or 1 µg/ml rabbit anti-Myc Ab (Sigma-Aldrich) for 1 h and then washed twice in ice-cold PBS before fixation. In some experiments, the cells were subsequently permeabilized and incubated with a different Ab to detect an intracellular protein such as the $Ca_vβ$ subunits and EGFP-$Ca_v1.2$ in the same cells. Visualization by immunofluorescence microscopy was as described in the previous section.

Quantification of surface channel expression was performed as follows: a random 540 × 540–µm area was scanned for each coverslip at 488 nm (EGFP-$Ca_v1.2$ cell expression), 546 nm ($Ca_v1.2$ surface expression), and 633 nm (N-Myc–BARP surface expression) using a microscope (Eclipse Ti; Nikon; 20×, 1.0 NA oil objective) with a motorized stage with NIS element AR software version 4.0 (Nikon). Cells expressing $Ca_v1.2$ alone or with $Ca_vβ3$ were first selected blindly based on EGFP fluorescence only (reflecting $Ca_v1.2$ total expression) and segmented, without looking at the surface expression. The mask thus defined was then applied to all fluorophores, and mean pixel intensity for each cell was calculated, yielding $Ca_v1.2$ total expression (488 nm) and relative surface localization (546/488 nm). Cell surface expression of $Ca_v1.2$ with $Ca_vβ3$ together with BARP WT or domain I and II mutated was performed by first blindly selecting cells expressing BARP (633 nm), without looking at the total or surface expression of EGFP-$Ca_v1.2$. Again, the thus defined regions of interest were used as a mask to measure mean pixel intensity for each cell and each channel. To ascertain that quantification is not affected by Cav1.2 cellular expression, a cutoff corresponding to half of the mean pixel intensity of EGFP-$Ca_v1.2$ in the absence of BARP was applied.

Colocalization analysis

Fluorescence colocalization was quantified using the ImageJ/Fiji (National Institutes of Health; Schneider et al., 2012) with the plugin Coloc 2 (version December 2011), after confocal image acquisition with 62-nm/pixel spatial oversampling (FluoView FV1000 confocal with 100×, 1.4 NA oil objective, software version 4.0). For each cell, five independent optical sections were acquired at low noise (Kalman filter 5), sequentially for each channel, with negligible bleed through between channels. For accurate sampling of the different cell compartments, the five sections were projected into single images (one per channel) before background subtraction and colocalization analysis. Region of interest was defined automatically by applying a logical OR operation the two segmented channels, to select pixels that are above background in each channel. The colocalization index is reported as the thresholded Pearson's correlation coefficient, as it is more robust than other metrics (Adler and Parmryd, 2010). For each condition, at least 13–30 cells from three independent replicates were analyzed.

Electrophysiology

Whole-cell patch clamp recordings were made on BHK, PC12, and tsA201 cells using bath solution containing 40 mM Ba^{2+} at 37°C as previously described (Béguin et al., 2001, 2006). In brief, to obtain expression of EGFP and BARP, the WT or mutated BARP cDNAs were transfected into the P/Q or N type–expressing BHK cell lines or PC12 cells using the pCMS-EGFP vector (Takara Bio Inc.). Cells expressing the EGFP were selected for measurements. For expression in the tsA201 cells, WT and mutated BARP cDNA were cloned into a pCMS-EGFP vector in which EGFP had been replaced by mCherry and cotransfected with a pCMS-EGFP vector carrying the cDNAs for $Ca_v1.2$ and $Ca_vβ3$ separated by an internal ribosomal entry site. Cells expressing EGFP and mCherry were selected for measurements. For each cell, current density (I_{Ba}) was calculated by dividing the total current by the membrane capacitance. The holding potential was –60 mV, and test pulses of 400 ms at potentials between −40 and 60 mV in steps of 10 mV were applied every 4 s. The membrane potential was measured by the perforated patch clamp method in the current clamp mode as previously described (Gonoi et al., 1994).

Growth hormone secretion and membrane potential

Secretion of transfected human growth hormone (hGH) or acetylcholine by PC12 cells were assayed as described previously (Béguin et al., 2001; Kiyonaka et al., 2007). In brief, PC12 cells were cotransfected with pXGH5 vector (Nichols Institute) containing an SRα promoter driving WT or mutated BARP, using Lipofectamine (Invitrogen) according to the manufacturer's instructions. After 3 d, PC12 cells were washed with a physiological salt solution (PSS; 140 mM NaCl, 4.7 mM KCl, 2.5 mM $CaCl_2$, 1.2 mM $MgCl_2$, 1.2 mM KH_2PO_4, 20 mM Hepes, pH 7.4, and 11 mM glucose) and incubated for 10 min with a high K^+ solution (PSS containing 60 mM KCl and 85 mM NaCl) or a low K^+ solution (PSS containing 4.7 mM KCl and 140 mM NaCl). Growth hormone was measured with a colorimetric immunoassay kit (Roche). Acetylcholine secretion in PC12 cells (Kiyonaka et al., 2007) was assayed with the similar basic procedure with the exception that pXGH5 was replaced by pEFmChAT cDNA, and acetylcholine release was measured using HPLC with electrochemical detection (HTEC-500; EiCOM).

Molecular modeling

In silico modeling, molecular dynamics, and energy refinements were performed using the Sybyl 7.2 software package (Tripos, Inc.). The $Ca_vβ$ subunit crystal structure (Protein Data Bank accession no. 1VYT) was used as a template to dock the BARP domain I. This domain was modeled as an α helix in a reverse orientation. Amino acid W427 of BARP was positioned similarly to residue W440 of AID followed by molecular dynamics simulations (1,000 fs with 1-fs steps at 300 K) between residues of the $Ca_vβ$ subunit and domain I within 6 Å. The lowest energy conformation was then obtained by energy minimization using Powell's method (Fletcher and Powell, 1963). The α-helical model of domain I shown in Fig. S3 D was generated using Phyre2 (Kelley and Sternberg, 2009).

Data and statistical analysis

Statistical significances were tested using unpaired and paired Student's *t* tests, and results were expressed as means ± SEM for the indicated *n* values. For coprecipitation, pull-down, WB, and immunofluorescence microscopy experiments, at least three independent experiments were performed, and a representative example is shown.

Online supplemental material

Fig. S1 shows alignment of BARP protein sequences of different species, evidence for the specificity of antibodies to BARP, and the assignment of the initiation methionine and glycosylation of BARP. Fig. S2 shows expression of BARP during mouse development, evidence for the specificity of the antibodies for immunohistochemistry localization of BARP in brain and pancreas, localization of overexpressed BARP and overexpressed synaptotagmin I, and membrane localization of $Ca_vβ$ subunit isoforms by BARP. Fig. S3 shows the identification of domains and amino acids in BARP that mediate the interaction with $Ca_vβ$ and molecular dynamics modeling of the interaction of BARP domain I with the ABP of $Ca_vβ$. Fig. S4 characterizes the effect of BARP on the association of the $Ca_vβ$ with the $Ca_vα1$ subunit and the association of BARP with different $Ca_vβ$ subunit isoforms in brain. Fig. S5 analyzes the effect of BARP on VGCC activity and surface expression and presents a working model for BARP as a $Ca_vβ$-anchoring protein. Online supplemental material is available at http://www.jcb.org/cgi/content/full/jcb.201304101/DC1.

We gratefully acknowledge the technical support from the Support Unit for Bio-Material Analysis, Brain Science Institute Research Resources Center for DNA sequencing and cell sorting and the Institute of Molecular and Cell Biology DNA Sequencing Facility for DNA sequencing.

This work was supported by the Agency for Science, Technology and Research, Singapore and the RIKEN Brain Science Institute, Japan.

The authors declare no competing financial interests.

Submitted: 16 April 2013
Accepted: 17 March 2014

Published April 21, 2014

References

Adler, J., and I. Parmryd. 2010. Quantifying colocalization by correlation: the Pearson correlation coefficient is superior to the Mander's overlap coefficient. *Cytometry A.* 77A:733–742. http://dx.doi.org/10.1002/cyto.a.20896

Altier, C., S.J. Dubel, C. Barrère, S.E. Jarvis, S.C. Stotz, R.L. Spaetgens, J.D. Scott, V. Cornet, M. De Waard, G.W. Zamponi, et al. 2002. Trafficking of L-type calcium channels mediated by the postsynaptic scaffolding protein AKAP79. *J. Biol. Chem.* 277:33598–33603. http://dx.doi.org/10.1074/jbc.M202476200

Altier, C., A. García-Caballero, B. Simms, H. You, L. Chen, J. Walcher, H.W. Tedford, T. Hermosilla, and G.W. Zamponi. 2011. The Cavβ subunit prevents RFP2-mediated ubiquitination and proteasomal degradation of L-type channels. *Nat. Neurosci.* 14:173–180. http://dx.doi.org/10.1038/nn.2712

Arikkath, J., and K.P. Campbell. 2003. Auxiliary subunits: essential components of the voltage-gated calcium channel complex. *Curr. Opin. Neurobiol.* 13:298–307. http://dx.doi.org/10.1016/S0959-4388(03)00066-7

Atiya-Nasagi, Y., H. Cohen, O. Medalia, M. Fukudan, and R. Sagi-Eisenberg. 2005. O-glycosylation is essential for intracellular targeting of synaptotagmins I and II in non-neuronal specialized secretory cells. *J. Cell Sci.* 118:1363–1372. http://dx.doi.org/10.1242/jcs.01710

Atwood, H.L. 2006. Neuroscience. Gatekeeper at the synapse. *Science.* 312:1008–1009. http://dx.doi.org/10.1126/science.1128445

Beedle, A.M., J.E. McRory, O. Poirot, C.J. Doering, C. Altier, C. Barrere, J. Hamid, J. Nargeot, E. Bourinet, and G.W. Zamponi. 2004. Agonist-independent modulation of N-type calcium channels by ORL1 receptors. *Nat. Neurosci.* 7:118–125. http://dx.doi.org/10.1038/nn1180

Béguin, P., K. Nagashima, T. Gonoi, T. Shibasaki, K. Takahashi, Y. Kashima, N. Ozaki, K. Geering, T. Iwanaga, and S. Seino. 2001. Regulation of Ca2+ channel expression at the cell surface by the small G-protein kir/Gem. *Nature.* 411:701–706. http://dx.doi.org/10.1038/35079621

Béguin, P., R.N. Mahalakshmi, K. Nagashima, D.H. Cher, N. Kuwamura, Y. Yamada, Y. Seino, and W. Hunziker. 2005a. Roles of 14-3-3 and calmodulin binding in subcellular localization and function of the small G-protein Rem2. *Biochem. J.* 390:67–75. http://dx.doi.org/10.1042/BJ20050414

Béguin, P., R.N. Mahalakshmi, K. Nagashima, D.H. Cher, A. Takahashi, Y. Yamada, Y. Seino, and W. Hunziker. 2005b. 14-3-3 and calmodulin control subcellular distribution of Kir/Gem and its regulation of cell shape and calcium channel activity. *J. Cell Sci.* 118:1923–1934. http://dx.doi.org/10.1242/jcs.02321

Béguin, P., R.N. Mahalakshmi, K. Nagashima, D.H. Cher, H. Ikeda, Y. Yamada, Y. Seino, and W. Hunziker. 2006. Nuclear sequestration of beta-subunits by Rad and Rem is controlled by 14-3-3 and calmodulin and reveals a novel mechanism for Ca2+ channel regulation. *J. Mol. Biol.* 355:34–46. http://dx.doi.org/10.1016/j.jmb.2005.10.013

Béguin, P., Y.J. Ng, C. Krause, R.N. Mahalakshmi, M.Y. Ng, and W. Hunziker. 2007. RGK small GTP-binding proteins interact with the nucleotide kinase domain of Ca2+-channel beta-subunits via an uncommon effector binding domain. *J. Biol. Chem.* 282:11509–11520. http://dx.doi.org/10.1074/jbc.M606423200

Bell, D.C., A.J. Butcher, N.S. Berrow, K.M. Page, P.F. Brust, A. Nesterova, K.A. Stauderman, G.R. Seabrook, B. Nürnberg, and A.C. Dolphin. 2001. Biophysical properties, pharmacology, and modulation of human, neuronal L-type (alpha(1D), Ca(V)1.3) voltage-dependent calcium currents. *J. Neurophysiol.* 85:816–827.

Bezprozvanny, I., R.H. Scheller, and R.W. Tsien. 1995. Functional impact of syntaxin on gating of N-type and Q-type calcium channels. *Nature.* 378:623–626. http://dx.doi.org/10.1038/378623a0

Bidaud, I., A. Mezghrani, L.A. Swayne, A. Monteil, and P. Lory. 2006. Voltage-gated calcium channels in genetic diseases. *Biochim. Biophys. Acta.* 1763:1169–1174. http://dx.doi.org/10.1016/j.bbamcr.2006.08.049

Brice, N.L., N.S. Berrow, V. Campbell, K.M. Page, K. Brickley, I. Tedder, and A.C. Dolphin. 1997. Importance of the different beta subunits in the membrane expression of the alpha1A and alpha2 calcium channel subunits: studies using a depolarization-sensitive alpha1A antibody. *Eur. J. Neurosci.* 9:749–759. http://dx.doi.org/10.1111/j.1460-9568.1997.tb01423.x

Buraei, Z., and J. Yang. 2010. The ß subunit of voltage-gated Ca2+ channels. *Physiol. Rev.* 90:1461–1506. http://dx.doi.org/10.1152/physrev.00057.2009

Cantí, C., A. Davies, N.S. Berrow, A.J. Butcher, K.M. Page, and A.C. Dolphin. 2001. Evidence for two concentration-dependent processes for beta-subunit effects on alpha1B calcium channels. *Biophys. J.* 81:1439–1451. http://dx.doi.org/10.1016/S0006-3495(01)75799-2

Catterall, W.A. 2000. Structure and regulation of voltage-gated Ca2+ channels. *Annu. Rev. Cell Dev. Biol.* 16:521–555. http://dx.doi.org/10.1146/annurev.cellbio.16.1.521

Chen, H., H.L. Puhl III, S.L. Niu, D.C. Mitchell, and S.R. Ikeda. 2005. Expression of Rem2, an RGK family small GTPase, reduces N-type calcium current without affecting channel surface density. *J. Neurosci.* 25:9762–9772. http://dx.doi.org/10.1523/JNEUROSCI.3111-05.2005

Chen, Y.H., M.H. Li, Y. Zhang, L.L. He, Y. Yamada, A. Fitzmaurice, Y. Shen, H. Zhang, L. Tong, and J. Yang. 2004. Structural basis of the alpha1-beta subunit interaction of voltage-gated Ca2+ channels. *Nature.* 429:675–680. http://dx.doi.org/10.1038/nature02641

Chen, Y., B. Stevens, J. Chang, J. Milbrandt, B.A. Barres, and J.W. Hell. 2008. NS21: re-defined and modified supplement B27 for neuronal cultures. *J. Neurosci. Methods.* 171:239–247. http://dx.doi.org/10.1016/j.jneumeth.2008.03.013

Chien, A.J., X. Zhao, R.E. Shirokov, T.S. Puri, C.F. Chang, D. Sun, E. Rios, and M.M. Hosey. 1995. Roles of a membrane-localized beta subunit in the formation and targeting of functional L-type Ca2+ channels. *J. Biol. Chem.* 270:30036–30044. http://dx.doi.org/10.1074/jbc.270.50.30036

Christopherson, K.S., E.M. Ullian, C.C. Stokes, C.E. Mullowney, J.W. Hell, A. Agah, J. Lawler, D.F. Mosher, P. Bornstein, and B.A. Barres. 2005. Thrombospondins are astrocyte-secreted proteins that promote CNS synaptogenesis. *Cell.* 120:421–433. http://dx.doi.org/10.1016/j.cell.2004.12.020

Colecraft, H.M., B. Alseikhan, S.X. Takahashi, D. Chaudhuri, S. Mittman, V. Yegnasubramanian, R.S. Alvania, D.C. Johns, E. Marbán, and D.T. Yue. 2002. Novel functional properties of Ca(2+) channel beta subunits revealed by their expression in adult rat heart cells. *J. Physiol.* 541:435–452. http://dx.doi.org/10.1113/jphysiol.2002.018515

De Waard, M., D.R. Witcher, M. Pragnell, H. Liu, and K.P. Campbell. 1995. Properties of the α1-β anchoring site in voltage-dependent Ca2+ channels. *J. Biol. Chem.* 270:12056–12064. http://dx.doi.org/10.1074/jbc.270.20.12056

Dieni, S., T. Matsumoto, M. Dekkers, S. Rauskolb, M.S. Ionescu, R. Deogracias, E.D. Gundelfinger, M. Kojima, S. Nestel, M. Frotscher, and Y.A. Barde. 2012. BDNF and its pro-peptide are stored in presynaptic dense core vesicles in brain neurons. *J. Cell Biol.* 196:775–788. http://dx.doi.org/10.1083/jcb.201201038

Dolphin, A.C. 2003. Beta subunits of voltage-gated calcium channels. *J. Bioenerg. Biomembr.* 35:599–620. http://dx.doi.org/10.1023/B:JOBB.0000008026.37790.5a

Evans, R.M., and G.W. Zamponi. 2006. Presynaptic Ca2+ channels—integration centers for neuronal signaling pathways. *Trends Neurosci.* 29:617–624. http://dx.doi.org/10.1016/j.tins.2006.08.006

Fan, M., Z. Buraei, H.R. Luo, R. Levenson-Palmer, and J. Yang. 2010. Direct inhibition of P/Q-type voltage-gated Ca2+ channels by Gem does not require a direct Gem/Cavbeta interaction. *Proc. Natl. Acad. Sci. USA.* 107:14887–14892. http://dx.doi.org/10.1073/pnas.1007543107

Finlin, B.S., A.L. Mosley, S.M. Crump, R.N. Correll, S. Ozcan, J. Satin, and D.A. Andres. 2005. Regulation of L-type Ca2+ channel activity and insulin secretion by the Rem2 GTPase. *J. Biol. Chem.* 280:41864–41871. http://dx.doi.org/10.1074/jbc.M414261200

Fletcher, R., and M.D.J. Powell. 1963. A rapidly convergent descent method for minimization. *Comput. J.* 6:163–168. http://dx.doi.org/10.1093/comjnl/6.2.163

Flynn, R., and G.W. Zamponi. 2010. Regulation of calcium channels by RGK proteins. *Channels (Austin).* 4:434–439. http://dx.doi.org/10.4161/chan.4.6.12865

Fujita, Y., M. Mynlieff, R.T. Dirksen, M.S. Kim, T. Niidome, J. Nakai, T. Friedrich, N. Iwabe, T. Miyata, T. Furuichi, et al. 1993. Primary structure and functional expression of the omega-conotoxin-sensitive N-type calcium channel from rabbit brain. *Neuron.* 10:585–598. http://dx.doi.org/10.1016/0896-6273(93)90162-K

Gandini, M.A., A. Sandoval, R. González-Ramírez, Y. Mori, M. de Waard, and R. Felix. 2011. Functional coupling of Rab3-interacting molecule 1 (RIM1) and L-type Ca2+ channels in insulin release. *J. Biol. Chem.* 286:15757–15765. http://dx.doi.org/10.1074/jbc.M110.187757

Geib, S., G. Sandoz, K. Mabrouk, A. Matavel, P. Marchot, T. Hoshi, M. Villaz, M. Ronjat, R. Miquelis, C. Lévêque, and M. de Waard. 2002. Use of a purified and functional recombinant calcium-channel beta4 subunit in surface-plasmon resonance studies. *Biochem. J.* 364:285–292.

Gerhard, D.S., L. Wagner, E.A. Feingold, C.M. Shenmen, L.H. Grouse, G. Schuler, S.L. Klein, S. Old, R. Rasooly, P. Good, et al.; MGC Project Team. 2004. The status, quality, and expansion of the NIH full-length cDNA project: the Mammalian Gene Collection (MGC). *Genome Res.* 14:2121–2127. http://dx.doi.org/10.1101/gr.2596504

Gonoi, T., N. Mizuno, N. Inagaki, H. Kuromi, Y. Seino, J. Miyazaki, and S. Seino. 1994. Functional neuronal ionotropic glutamate receptors are expressed in the non-neuronal cell line MIN6. *J. Biol. Chem.* 269:16989–16992.

Han, W., J.S. Rhee, A. Maximov, Y. Lao, T. Mashimo, C. Rosenmund, and T.C. Südhof. 2004. N-glycosylation is essential for vesicular targeting of synaptotagmin 1. *Neuron.* 41:85–99. http://dx.doi.org/10.1016/S0896-6273(03)00820-1

Published April 21, 2014

Herlitze, S., D.E. Garcia, K. Mackie, B. Hille, T. Scheuer, and W.A. Catterall. 1996. Modulation of Ca2+ channels by G-protein βγ subunits. *Nature*. 380:258–262. http://dx.doi.org/10.1038/380258a0

Hidalgo, P., G. Gonzalez-Gutierrez, J. Garcia-Olivares, and A. Neely. 2006. The alpha1-beta-subunit interaction that modulates calcium channel activity is reversible and requires a competent alpha-interaction domain. *J. Biol. Chem.* 281:24104–24110. http://dx.doi.org/10.1074/jbc.M605930200

Ikeda, S.R. 1996. Voltage-dependent modulation of N-type calcium channels by G-protein beta gamma subunits. *Nature*. 380:255–258. http://dx.doi.org/10.1038/380255a0

Jarvis, S.E., and G.W. Zamponi. 2007. Trafficking and regulation of neuronal voltage-gated calcium channels. *Curr. Opin. Cell Biol.* 19:474–482. http://dx.doi.org/10.1016/j.ceb.2007.04.020

Jones, L.P., S.K. Wei, and D.T. Yue. 1998. Mechanism of auxiliary subunit modulation of neuronal alpha1E calcium channels. *J. Gen. Physiol.* 112:125–143. http://dx.doi.org/10.1085/jgp.112.2.125

Josephson, I.R., and G. Varadi. 1996. The beta subunit increases Ca2+ currents and gating charge movements of human cardiac L-type Ca2+ channels. *Biophys. J.* 70:1285–1293. http://dx.doi.org/10.1016/S0006-3495(96)79685-6

Kameyama, K., K. Aono, and K. Kitamura. 1999. Isoflurane inhibits neuronal Ca2+ channels through enhancement of current inactivation. *Br. J. Anaesth.* 82:402–411. http://dx.doi.org/10.1093/bja/82.3.402

Kamp, T.J., M.T. Pérez-García, and E. Marban. 1996. Enhancement of ionic current and charge movement by coexpression of calcium channel beta 1A subunit with alpha 1C subunit in a human embryonic kidney cell line. *J. Physiol.* 492:89–96.

Kang, M.G., C.C. Chen, M. Wakamori, Y. Hara, Y. Mori, and K.P. Campbell. 2006. A functional AMPA receptor-calcium channel complex in the postsynaptic membrane. *Proc. Natl. Acad. Sci. USA*. 103:5561–5566. http://dx.doi.org/10.1073/pnas.0601289103

Kelley, L.A., and M.J. Sternberg. 2009. Protein structure prediction on the Web: a case study using the Phyre server. *Nat. Protoc.* 4:363–371. http://dx.doi.org/10.1038/nprot.2009.2

Kiyonaka, S., M. Wakamori, T. Miki, Y. Uriu, M. Nonaka, H. Bito, A.M. Beedle, E. Mori, Y. Hara, M. De Waard, et al. 2007. RIM1 confers sustained activity and neurotransmitter vesicle anchoring to presynaptic Ca2+ channels. *Nat. Neurosci.* 10:691–701. http://dx.doi.org/10.1038/nn1904

Launey, T., S. Endo, R. Sakai, J. Harano, and M. Ito. 2004. Protein phosphatase 2A inhibition induces cerebellar long-term depression and declustering of synaptic AMPA receptor. *Proc. Natl. Acad. Sci. USA*. 101:676–681. http://dx.doi.org/10.1073/pnas.0302914101

Lee, A., S.T. Wong, D. Gallagher, B. Li, D.R. Storm, T. Scheuer, and W.A. Catterall. 1999. Ca2+/calmodulin binds to and modulates P/Q-type calcium channels. *Nature*. 399:155–159. http://dx.doi.org/10.1038/20194

Mahalakshmi, R.N., K. Nagashima, M.Y. Ng, N. Inagaki, W. Hunziker, and P. Béguin. 2007a. Nuclear transport of Kir/Gem requires specific signals and importin alpha5 and is regulated by calmodulin and predicted serine phosphorylations. *Traffic*. 8:1150–1163. http://dx.doi.org/10.1111/j.1600-0854.2007.00598.x

Mahalakshmi, R.N., M.Y. Ng, K. Guo, Z. Qi, W. Hunziker, and P. Béguin. 2007b. Nuclear localization of endogenous RGK proteins and modulation of cell shape remodeling by regulated nuclear transport. *Traffic*. 8:1164–1178. http://dx.doi.org/10.1111/j.1600-0854.2007.00599.x

Maximov, A., and I. Bezprozvanny. 2002. Synaptic targeting of N-type calcium channels in hippocampal neurons. *J. Neurosci.* 22:6939–6952.

Mori, Y., T. Friedrich, M.S. Kim, A. Mikami, J. Nakai, P. Ruth, E. Bosse, F. Hofmann, V. Flockerzi, T. Furuichi, et al. 1991. Primary structure and functional expression from complementary DNA of a brain calcium channel. *Nature*. 350:398–402. http://dx.doi.org/10.1038/350398a0

Neher, E. 1998. Vesicle pools and Ca2+ microdomains: new tools for understanding their roles in neurotransmitter release. *Neuron*. 20:389–399. http://dx.doi.org/10.1016/S0896-6273(00)80983-6

Niidome, T., T. Teramoto, Y. Murata, I. Tanaka, T. Seto, K. Sawada, Y. Mori, and K. Katayama. 1994. Stable expression of the neuronal BI (class A) calcium channel in baby hamster kidney cells. *Biochem. Biophys. Res. Commun.* 203:1821–1827. http://dx.doi.org/10.1006/bbrc.1994.2399

Nishimune, H., J.R. Sanes, and S.S. Carlson. 2004. A synaptic laminin-calcium channel interaction organizes active zones in motor nerve terminals. *Nature*. 432:580–587. http://dx.doi.org/10.1038/nature03112

Obermair, G.J., B. Schlick, V. Di Biase, P. Subramanyam, M. Gebhart, S. Baumgartner, and B.E. Flucher. 2010. Reciprocal interactions regulate targeting of calcium channel beta subunits and membrane expression of alpha1 subunits in cultured hippocampal neurons. *J. Biol. Chem.* 285:5776–5791. http://dx.doi.org/10.1074/jbc.M109.044271

Opatowsky, Y., O. Chomsky-Hecht, M.G. Kang, K.P. Campbell, and J.A. Hirsch. 2003. The voltage-dependent calcium channel beta subunit contains two stable interacting domains. *J. Biol. Chem.* 278:52323–52332. http://dx.doi.org/10.1074/jbc.M303564200

Opatowsky, Y., C.C. Chen, K.P. Campbell, and J.A. Hirsch. 2004. Structural analysis of the voltage-dependent calcium channel beta subunit functional core and its complex with the alpha 1 interaction domain. *Neuron*. 42:387–399. http://dx.doi.org/10.1016/S0896-6273(04)00250-8

Pragnell, M., M. De Waard, Y. Mori, T. Tanabe, T.P. Snutch, and K.P. Campbell. 1994. Calcium channel beta-subunit binds to a conserved motif in the I-II cytoplasmic linker of the alpha 1-subunit. *Nature*. 368:67–70. http://dx.doi.org/10.1038/368067a0

Pruitt, K.D., J. Harrow, R.A. Harte, C. Wallin, M. Diekhans, D.R. Maglott, S. Searle, C.M. Farrell, J.E. Loveland, B.J. Ruef, et al. 2009. The consensus coding sequence (CCDS) project: Identifying a common protein-coding gene set for the human and mouse genomes. *Genome Res.* 19:1316–1323. http://dx.doi.org/10.1101/gr.080531.108

Richards, M.W., A.J. Butcher, and A.C. Dolphin. 2004. Ca2+ channel beta-subunits: structural insights AID our understanding. *Trends Pharmacol. Sci.* 25:626–632. http://dx.doi.org/10.1016/j.tips.2004.10.008

Schneider, C.A., W.S. Rasband, and K.W. Eliceiri. 2012. NIH Image to ImageJ: 25 years of image analysis. *Nat. Methods*. 9:671–675. http://dx.doi.org/10.1038/nmeth.2089

Sheng, Z.H., J. Rettig, M. Takahashi, and W.A. Catterall. 1994. Identification of a syntaxin-binding site on N-type calcium channels. *Neuron*. 13:1303–1313. http://dx.doi.org/10.1016/0896-6273(94)90417-0

Spafford, J.D., and G.W. Zamponi. 2003. Functional interactions between presynaptic calcium channels and the neurotransmitter release machinery. *Curr. Opin. Neurobiol.* 13:308–314. http://dx.doi.org/10.1016/S0959-4388(03)00061-8

Ullian, E.M., K.S. Christopherson, and B.A. Barres. 2004. Role for glia in synaptogenesis. *Glia*. 47:209–216. http://dx.doi.org/10.1002/glia.20082

Van Petegem, F., K.A. Clark, F.C. Chatelain, and D.L. Minor Jr. 2004. Structure of a complex between a voltage-gated calcium channel beta-subunit and an alpha-subunit domain. *Nature*. 429:671–675. http://dx.doi.org/10.1038/nature02588

Vega, I.E., and S.C. Hsu. 2001. The exocyst complex associates with microtubules to mediate vesicle targeting and neurite outgrowth. *J. Neurosci.* 21:3839–3848.

Weiss, N., A. Sandoval, S. Kyonaka, R. Felix, Y. Mori, and M. De Waard. 2011. Rim1 modulates direct G-protein regulation of Ca(v)2.2 channels. *Pflugers Arch.* 461:447–459. http://dx.doi.org/10.1007/s00424-011-0926-5

Yang, S.N., and P.O. Berggren. 2006. The role of voltage-gated calcium channels in pancreatic beta-cell physiology and pathophysiology. *Endocr. Rev.* 27:621–676. http://dx.doi.org/10.1210/er.2005-0888

Yang, T., X. Xu, T. Kernan, V. Wu, and H.M. Colecraft. 2010. Rem, a member of the RGK GTPases, inhibits recombinant CaV1.2 channels using multiple mechanisms that require distinct conformations of the GTPase. *J. Physiol.* 588:1665–1681. http://dx.doi.org/10.1113/jphysiol.2010.187203

Zhai, R.G., and H.J. Bellen. 2004. The architecture of the active zone in the presynaptic nerve terminal. *Physiology (Bethesda)*. 19:262–270. http://dx.doi.org/10.1152/physiol.00014.2004

Zhong, H., C.T. Yokoyama, T. Scheuer, and W.A. Catterall. 1999. Reciprocal regulation of P/Q-type Ca2+ channels by SNAP-25, syntaxin and synaptotagmin. *Nat. Neurosci.* 2:939–941. http://dx.doi.org/10.1038/14721

Metabolism:

Glucose-stimulated single pancreatic islets sustain increased cytosolic ATP levels during initial Ca2+ influx and subsequent Ca2+ oscillations

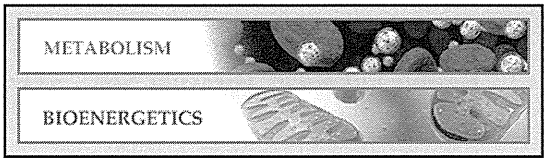

Takashi Tanaka, Kazuaki Nagashima, Nobuya Inagaki, Hidetaka Kioka, Seiji Takashima, Hajime Fukuoka, Hiroyuki Noji, Akira Kakizuka and Hiromi Imamura

J. Biol. Chem. published online December 3, 2013

JBC Papers in Press. Published on December 3, 2013 as Manuscript M113.499111
The latest version is at http://www.jbc.org/cgi/doi/10.1074/jbc.M113.499111

Glucose-stimulated single pancreatic islets sustain increased cytosolic ATP levels during initial Ca^{2+} influx and subsequent Ca^{2+} oscillations.

Takashi Tanaka[*], Kazuaki Nagashima[†], Nobuya Inagaki[†], Hidetaka Kioka[‡], Seiji Takashima[‡], Hajime Fukuoka[§], Hiroyuki Noji[¶], Akira Kakizuka[*], and Hiromi Imamura[*, ‖, 1]

[*]Graduate School of Biostudies, Kyoto University, Kyoto, Japan
[†]Graduate School of Medicine, Kyoto University, Kyoto, Japan
[‡]Graduate School of Medicine, Osaka University, Suita, Japan
[§]Institute of Multidisciplinary Research for Advanced Materials, Tohoku University, Sendai, Japan
[¶]Department of Applied Chemistry, University of Tokyo, Tokyo, Japan
[‖]The Hakubi Center for Advanced Research, Kyoto University, Kyoto, Japan.

Running title: *Dynamics of intracellular ATP levels in pancreatic islets*

[1]To whom correspondence should be addressed to H.I. (Tel.: 81-75-753-7681; Fax: 81-75-753-7676; E-mail: imamura@lif.kyoto-u.ac.jp).

Key words: ATP; calcium; energy metabolism; imaging; insulin; pancreatic islets

Background: The roles of ATP in glucose-stimulated insulin secretion have not been well described.
Results: After glucose stimulation, ATP levels were elevated prior to an increase in Ca^{2+} levels. High non-oscillatory ATP levels were sustained during Ca^{2+} oscillations.
Conclusion: High ATP levels may be necessary for initial Ca^{2+} influx and subsequent Ca^{2+} oscillations.
Significance: This adds new insight into the mechanism of insulin secretion.

ABSTRACT

In pancreatic islets, insulin secretion occurs via synchronous elevation of Ca^{2+} levels throughout the islets during high glucose conditions. This Ca^{2+} elevation has two phases; a quick increase, observed after the glucose stimulus, followed by prolonged oscillations. In these processes, the elevation of intracellular ATP levels generated from glucose is assumed to inhibit ATP-sensitive K^+ channels, leading to the depolarization of membranes, which in turn induces Ca^{2+} elevation in the islets. However, little is known about the dynamics of intracellular ATP levels and their correlation with Ca^{2+} levels in the islets in response to changing glucose levels. In this study, a genetically encoded fluorescent biosensor for ATP and a fluorescent Ca^{2+} dye were employed to simultaneously monitor the dynamics of intracellular ATP and Ca^{2+} levels, respectively, inside single isolated islets. We observed rapid increases in cytosolic and mitochondrial ATP levels after stimulation with glucose, as well as

with methyl pyruvate or leucine/glutamine. High ATP levels were sustained as long as high glucose levels persisted. Inhibition of ATP production suppressed the initial Ca^{2+} increase, suggesting that enhanced energy metabolism triggers the initial phase of Ca^{2+} influx. On the other hand, cytosolic ATP levels did not fluctuate significantly with the Ca^{2+} level in the subsequent oscillation phases. Importantly, Ca^{2+} oscillations stopped immediately before ATP levels decreased significantly. These results might explain how food or glucose intake evokes insulin secretion, and how the resulting decrease in plasma glucose levels leads to cessation of secretion.

Multiple hormones control blood glucose levels. Among them, insulin, which is secreted from pancreatic β-cells, is the only hormone that can reduce blood glucose levels. It is thought that intracellular ATP is implicated in glucose-stimulated insulin secretion (GSIS). Specifically, the ATP-sensitive K^+ channel (K_{ATP} channel), which is closed by ATP, plays a critical role (1, 2). K_{ATP} channels in β-cells are composed of four Kir6.2 subunits, which form an inwardly rectifying K^+ channel, and four sulfonylurea receptor subunits (3, 4). Transgenic mice expressing a dominant-negative form of the Kir6.2 subunit in β-cells develop hypoglycemia with hyperinsulinemia in neonates and hyperglycemia with hypoinsulinemia, as well as a decreased β-cell population in adults (5). GSIS in mammals is assumed to begin with the uptake of glucose through the glucose transporter (GLUT), with a subsequent increase in cytosolic ATP levels ($[ATP]_c$) due to the metabolism of glucose through the glycolytic pathway and tri-carboxylic acid (TCA) cycle. Consequently, K^+ permeability is lowered by the closure of the K_{ATP} channel, resulting in the depolarization of the plasma membrane, followed by the influx of Ca^{2+} through voltage-dependent Ca^{2+} channels (VDCC) and a rapid increase in cytosolic Ca^{2+} levels ($[Ca^{2+}]_c$). It is known that insulin is secreted from β-cells in a synchronized manner with $[Ca^{2+}]_c$ (6), and that the dynamics of $[Ca^{2+}]_c$ in β-cells drastically change during GSIS. First, $[Ca^{2+}]_c$ increases in response to stimulation with high levels of glucose (the initial phase), and then starts to oscillate (the second phase) (6, 7, 8).

Although some studies have reported that intracellular ATP levels in β-cells do not increase upon glucose-stimulation (9, 10) and, thus, ADP or ATP/ADP ratio, rather than ATP, could be crucial for insulin secretion, there have also been many reports that support the increase in ATP (11, 12, 13). Because the turnover of intracellular ATP is quite rapid, ATP degradation could occur during extraction from the cells. Thus, ATP levels might be underestimated in the conventional ATP assay. To understand the actual dynamics of intracellular ATP during GSIS, a non-destructive method of measuring intracellular ATP is required. Recently, a genetically encoded fluorescent biosensor for the ATP/ADP ratio was employed in live pancreatic islets (14, 15). However, the dynamics of $[ATP]_c$ itself and its correlation with $[Ca^{2+}]_c$ in the initial phase have not been well investigated. Moreover, it remains unclear how $[ATP]_c$ couples with $[Ca^{2+}]_c$ oscillations in the second phase.

We previously developed the genetically encoded fluorescent ATP biosensors ATeam (16) and GO-ATeam (17), which are based on the principle of Förster resonance energy transfer (FRET) and insensitive to the related nucleotides, namely, ADP, GTP, and dATP (16, 17). Because

GO-ATeam has little spectral-overlap with the Ca^{2+}-sensitive dye fura-2, it has allowed us to monitor ATP levels and Ca^{2+} levels simultaneously in single living cells (17). In this paper, we visualized $[ATP]_c$ or mitochondrial ATP levels ($[ATP]_m$) together with $[Ca^{2+}]_c$ in each isolated islet by using GO-ATeam and fura-2, and examined how intracellular ATP dynamics regulate $[Ca^{2+}]_c$ in GSIS.

EXPERIMENTAL PROCEDURES

Chemicals – Carbonylcyanide 3-chlorophenylhydrazone (CCCP), methyl pyruvate and tolbutamide were purchased from Wako Chemicals (Osaka, Japan). Oligomycin A was purchased from Fluka (St. Louis, MO, USA). Fura-2-AM and BAPTA-AM were purchased from Dojindo (Tokyo, Japan). Iodoacetate was purchased from Sigma (St. Louis, MO, USA). Other chemicals were purchased from Nacalai Tesque (Kyoto, Japan) unless otherwise noted.

Isolation and culture of mouse pancreatic islets – Islets were isolated from the pancreases of C57BL/6J mice with the aid of collagenase (Roche) according to the general protocol. In brief, the pancreas was injected with a solution of 0.5 mg/mL collagenase via the bile duct. After collagenase digestion for 40 minutes at 37°C and 2 or 3 wash steps, density gradient centrifugation was performed using Ficoll. Islets were collected manually and cultured in RPMI 1640 (Nacalai Tesque) containing 11 mM glucose at 37°C in a humidified atmosphere containing 5% CO_2 for 2 to 3 days. The culture medium was supplemented with 10% fetal calf serum (Nichirei Biosciences Inc, Tokyo, Japan), 100 units/mL penicillin, and 100 μg/mL streptomycin.

Culture of MIN6 cells – Cells of the mouse insulinoma cell line MIN6 (18) were cultured in DMEM (Sigma) containing 25 mM glucose supplemented with 15% fetal bovine serum (Sigma), 55 μM 2-mercaptoethanol (GIBCO, Grand Island, NY, USA), 100 units/mL penicillin and 100 μg/mL streptomycin at 37°C in a humidified atmosphere containing 5% CO_2.

Generation of recombinant adenovirus - Adenovirus for the expression of GO-ATeam biosensors was generated using the ViraPower™ Adenoviral Expression System (Invitrogen, Carlsbad, CA, USA) according to the manufacturer's instructions. For construction of the adenoviral vector encoding GO-ATeam, the *Xho*I-*Pme*I fragment of pcDNA-GO-ATeam1 or pcDNA-mit-GO-ATeam1 (17) was subcloned into the pENTR-1A vector (Invitrogen), digested with *Sal*I and *Eco*RV, and then recombined into the pAd/CMV/V5-DEST destination vector.

Permeabilization of the plasma membrane - Plasma membranes of cells were permeabilized with 100 μg/mL α-hemolysin from *Staphylococcus aureus* (Sigma) for 30 minutes. After permeabilization, cells were perfused with intracellular-like medium containing 140 mM KCl, 6 mM NaCl, 1 mM $MgCl_2$, 0.465 mM $CaCl_2$, 2 mM EGTA and 12.5 mM HEPES (pH 7.0) and different concentrations of MgATP.

Imaging and data analysis - Islets were plated on a glass-bottom dish (Fine Plus International Ltd., Kyoto, Japan) and incubated at 37°C. For ATP imaging, ATeam1.03 (16) or a series of GO-ATeams (17) were transfected into islets using an adenoviral vector system. Before imaging, fura-2-AM was added to a final concentration of 2–5 μM for 30 minutes, and cells were preincubated in Krebs-Ringer-HEPES

(KRH) medium (119 mM NaCl, 4.74 mM KCl, 1.19 mM KH_2PO_4, 1.19 mM $MgCl_2$-$6H_2O$, 2.54 mM $CaCl_2$, 25 mM $NaHCO_3$, 10 mM HEPES, and 0.1 % BSA (pH 7.4) with 2.8 mM glucose) for 40 minutes. Wide-field observations of islets were performed on a Nikon Ti-E-PFS inverted microscope using a 40× objective (Nikon, Tokyo, Japan; CFI Super Fluor 40× oil: NA 1.30) and the following filter sets (Semrock, Rochester, NY, USA): for dual-emission ratio imaging of ATeam 1.03, 438/24 - DM458 - 483/32 (CFP) or 542/27 (YFP); for dual-emission ratio imaging of GO-ATeam, 482/18 - DM495 - 520/35 (GFP) or 579/34 (OFP); and for dual-excitation ratio imaging of fura-2, 340/26 (fura-2S) or 387/11 (fura-2L) - DM400 - 510/84. An ORCA-AG cooled CCD camera (Hamamatsu Photonics, Hamamatsu, Japan) was used to capture fluorescent images. The microscope system was controlled with NIS-Elements (Nikon). Imaging data were analyzed using MetaMorph (Molecular Devices, Sunnyvale, CA, USA). Certain parts of the islets were selected to quantify the average intensities of signals because of the non-uniform expression levels of ATP biosensors within an islet. Cross-correlation analysis was performed as reported previously (19).

RESULTS

Properties of GO-ATeam1 in insulin-secreting cells – The GO-ATeam1 biosensor is composed of the ε subunit of *Bacillus subtilis* F_oF_1-ATP synthase, a variant of *Aquoria* green fluorescent protein (GFP; cp173-mEGFP), and a variant of *Fungia* orange fluorescent protein (OFP; mKOκ) (17). By inducing a conformational change in the ε subunit, ATP binding to GO-ATeam1 increases FRET from GFP to OFP, thereby increasing the OFP/GFP emission ratio (FRET signal). To test whether GO-ATeam1 can sense ATP changes within insulin-secreting cells, we recorded FRET signals from GO-ATeam1-expressing MIN6 insulinoma cells, which were permeabilized with α-hemolysin. When the ATP concentration in the medium was altered, the FRET signal changed in an ATP concentration-dependent manner (Fig. 1A). Thus, GO-ATeam1 works properly in insulin-secreting cells. Moreover, we could monitor changes in the FRET signal when ATP levels were alternated between 7 mM and 8 mM (Fig. 1B), indicating that our system has the sensitivity to detect changes of intracellular ATP concentrations of 1 mM or less.

Dynamics of $[ATP]_c$ and $[ATP]_m$ in isolated islets upon high glucose stimulation – In order to monitor ATP dynamics in insulin-secreting cells, we first expressed the GO-ATeam1 fluorescent biosensor in the cytosol of MIN6 cells. Stimulation with 25 mM glucose induced a 5 ± 2% (mean ± S.D., n = 22) FRET signal increase in 73% of monitored MIN6 cells (Fig. 1C), although the remaining cells (27%) exhibited no changes in FRET signal due to unknown reasons.

We next expressed GO-ATeam1 in the cytosol of isolated mouse pancreatic islets. When a GO-ATeam1-expressing islet was stimulated by increasing the glucose concentration in the medium from low (2.8 mM) to high (25 mM), rapid increases in the FRET signal were observed (Fig. 2A). If factors besides ATP affect FRET signal of GO-ATeam1 independently of ATP binding, GO-ATeam3, which is an ATP-insensitive variant of GO-ATeam, will also show FRET changes. However, the FRET signal did not change in islets expressing GO-ATeam3 (Fig. 2B). Further, increases in FRET signal

(YFP/CFP emission ratio) were also observed in islets when ATeam1.03 was used instead of GO-ATeam1 (Fig. 2C). These results strongly suggest that the increase in FRET signal of GO-ATeam1 and ATeam1.03 after stimulation with high glucose levels is actually due to the increase in $[ATP]_c$. The time lag between glucose stimulation and the onset of FRET signal elevation was 22 ± 6 seconds (mean ± S.D., n = 13). After the rapid increase, $[ATP]_c$ remained high. When islets were stimulated with various concentrations of glucose, $[ATP]_c$ increased rapidly in a concentration-dependent manner (Fig. 2D). We were able to observe 6 ± 3, 13 ± 2, and 15 ± 3 % (mean ± S.D., n = 10 for each) increases in FRET signals when the same islets were treated with 8.3, 16.7, and 25 mM glucose, respectively (Fig. 2E). Because 25 mM glucose stimulation, which is supra-physiological, is the most effective condition in which to observe obvious increases in FRET signals, we decided to use 25 mM glucose for high glucose stimulation. When the glucose concentration in the medium was gradually increased in a stepwise manner, rather than abruptly, $[ATP]_c$ also increased gradually (Fig. 2F). The mean amplitude of the increased FRET signal with gradually increasing glucose concentrations was not much different from that seen with an abrupt increase in glucose. FRET signals from single cells of isolated islets were also monitored (Fig. 2G). At the single cell level, 25 mM glucose stimulation caused a 11 ± 3% (mean ± S.D., n = 11) increase in FRET signal, while oligomycin A treatment caused a 40 ± 3% decrease (mean ± S.D., n = 11), compared to basal levels.

Next, in order to examine whether mitochondrial energy metabolism is activated by glucose stimulation, FRET signals from a single islet expressing mitGO-ATeam1, a variant of GO-ATeam1 that is targeted to the mitochondrial matrix, were monitored. Like $[ATP]_c$, $[ATP]_m$ rapidly increased when islets were treated with 25 mM glucose (Fig. 2H), whereas the FRET signal of ATP-insensitive mitGO-ATeam3 did not change (Fig. 2I), indicating that mitGO-ATeam1 indeed reflected the activation of mitochondrial energy metabolism.

Next, we monitored $[ATP]_c$ while decreasing the glucose concentration in the medium. Figure 3A shows a representative time course of the FRET signal in an isolated pancreatic islet alternately subjected to 2.8 and 25 mM glucose. As expected, lowering the glucose concentration decreased $[ATP]_c$. Interestingly, the decrease in $[ATP]_c$ induced by glucose reduction was much slower than the increase in $[ATP]_c$ caused by glucose addition. This means that $[ATP]_c$ is much more responsive to an increase than a decrease in extracellular glucose. The average rate of FRET signal decline was about 6-fold slower than that of FRET signal increase (Fig. 3B). Specifically, the time required for the FRET signal to reach 50% of maximum was approximately 90 seconds after the addition of glucose, whereas approximately 340 seconds were required for the signal to fall to this level after reduction in glucose (Fig. 3C). This phenomenon is not due to the kinetic property of GO-ATeam1, because the time constants of purified GO-ATeam1 for ATP association/dissociation have been determined to be less than 10 seconds (17). Moreover, treatment with either iodoacetate, which inhibits glyceraldehyde-3-phosphate dehydrogenase in the glycolytic pathway, or oligomycin A, which inhibits F_oF_1-ATP synthase, rapidly reduced $[ATP]_c$ in pancreatic islets (Fig. 4), indicating that the time constants of GO-ATeam1 expressed in islets were also fast enough.

Dynamics of $[ATP]_c$ and $[Ca^{2+}]_c$ in glucose-stimulated islets – The fact that ATP can block K_{ATP} channels in physiological conditions strongly suggests a scenario where the increase in $[ATP]_c$, as a consequence of activated energy metabolism, is a first trigger of GSIS. This model assumes that $[ATP]_c$ increases prior to $[Ca^{2+}]_c$. In all islets investigated, elevations of $[ATP]_c$ always preceded those of $[Ca^{2+}]_c$ when islets were treated with 25 mM glucose (Fig. 5A, B). The time lag between the onset of $[ATP]_c$ and that of $[Ca^{2+}]_c$ increase was 96 ± 33 seconds (mean ± S.D., n = 19). This observation is consistent with two recent studies using Perceval, a genetically-encoded biosensor for the ATP/ADP ratio, in which the cytosolic ATP/ADP ratio increased prior to $[Ca^{2+}]_c$ in the initial phase in glucose-stimulated mouse islets (14, 15). Unlike the Perceval recording, however, we did not observe a transient drop in $[ATP]_c$ after glucose stimulation. It is noteworthy that the FRET signal of GO-ATeam is virtually unaffected by pH at physiological conditions (above pH 7), which is not the case for pH-sensitive Perceval. Moreover, although the reports using Perceval demonstrated that the ATP/ADP ratio increases prior to $[Ca^{2+}]_c$ in GSIS, they did not address whether the initial $[Ca^{2+}]_c$ increase can occur without the increase in ATP/ADP ratio or the actual $[ATP]_c$. To address this question, we investigated the effects of pharmacological inhibitors of energy metabolism on $[ATP]_c$ and $[Ca^{2+}]_c$ responses in glucose-stimulated islets. Pretreatment with either iodoacetate for about 6 minutes or oligomycin A for 1.5 to 3 minutes abrogated the glucose-induced $[ATP]_c$ increase, and, importantly, the subsequent $[Ca^{2+}]_c$ elevation (Fig. 5C, E). On the other hand, these inhibitor treatments did not abrogate the tolbutamide-induced elevation of $[Ca^{2+}]_c$ (Fig. 5D, F), indicating that the cells still sustained the ability to close K_{ATP} channels and open voltage-dependent calcium channels (VDCCs) immediately after treatment with iodoacetate or oligomycin A. These results indicate that the glucose-induced increase in energy metabolism depends entirely on both glycolysis and oxidative phosphorylation activity and is most likely crucial for subsequent Ca^{2+} elevation.

Dynamics of $[ATP]_c$ or $[ATP]_m$ together with $[Ca^{2+}]_c$ in methyl pyruvate-stimulated islets – We next investigated whether glucose-independent insulin secretion is also mediated by the activation of energy metabolism. Pyruvate, an end product of glycolysis, enters into mitochondria and is further metabolized through the TCA cycle after conversion to acetyl-CoA. However, stimulation with pyruvate does not lead to large effects on insulin secretion in isolated β-cells, presumably due to its low membrane permeability and the low expression levels of monocarboxylate transporter in isolated β-cells (20). On the other hand, the pyruvate analog methyl pyruvate (MP) is known to induce insulin secretion from isolated β-cells. Some reports have asserted that the insulinogenic effect of MP derives from its capacity to serve as a substrate for mitochondrial energy metabolism (21, 22), but others have suggested that MP directly affects K_{ATP} channels in a metabolism-independent manner (13, 23). These conflicting reports prompted us to test whether MP has a direct effect on ATP synthesis or not. Although MP decreased the pH of the medium from 7.4 to 7.0, the FRET signal of GO-ATeam is almost unaffected in this pH range (17). We stimulated islets with MP in the absence of

glucose and monitored $[ATP]_m$ or $[ATP]_c$ (Fig. 6A, B). MP induced rapid increases in $[ATP]_m$ and $[ATP]_c$, prior to an increase in $[Ca^{2+}]_c$, even when glucose was totally depleted from the medium. Next, we investigated the effects of oligomycin A on $[ATP]_c$ and $[Ca^{2+}]_c$ in MP-stimulated islets. Pretreatment with oligomycin A for 3 to 4 minutes abrogated the glucose-induced $[ATP]_c$ increase and the subsequent $[Ca^{2+}]_c$ elevation (Fig. 6C). These data strongly suggest that MP induces the influx of Ca^{2+} by increasing energy metabolism rather than directly affecting the K_{ATP} channel.

Dynamics of $[ATP]_c$ or $[ATP]_m$ together with $[Ca^{2+}]_c$ in leucine and glutamine-stimulated islets – Genetic data indicate that a mitochondrial enzyme, glutamate dehydrogenase (GDH), is important for insulin secretion. The constitutively active form of mutated GDH leads to hyperinsulinism syndrome (24), and deletion of GDH in β-cells partly impairs the insulin secretion response (25). GDH catalyzes the reversible reaction: glutamate + $NAD(P)^+$ ⟷ α-ketoglutarate + NH_4^+ + NAD(P)H. It is known that leucine is an allosteric activator of GDH and an inducer of insulin secretion in pancreatic β-cells (26, 27). We hypothesized that leucine activates GDH and induces increases in ATP via the TCA cycle by conversion to α-ketoglutarate, an intermediate of the TCA cycle. Thus, we stimulated isolated islets with leucine and monitored $[ATP]_m$ and $[ATP]_c$ together with $[Ca^{2+}]_c$. Treatment with leucine alone induced only slight increases in both $[ATP]_m$ and $[ATP]_c$, and did not trigger any increases in $[Ca^{2+}]_c$ (Fig. 7A, B). Likewise, glutamine stimulation alone did not induce changes in $[ATP]_m$ and $[ATP]_c$, or in $[Ca^{2+}]_c$ (Fig. 7C, D). Remarkably, when islets were pretreated with glutamine, stimulation with leucine led to an increase in both $[ATP]_m$ and $[ATP]_c$, followed by rapid elevation of $[Ca^{2+}]_c$ (Fig. 7E, F). Pretreatment with oligomycin A for just 3 to 5 minutes abrogated increases in $[ATP]_c$ when glutamine-pretreated islets were stimulated with leucine. Meanwhile, $[Ca^{2+}]_c$ gradually increased in parallel with the decrease in $[ATP]_c$ and did not rapidly increase after stimulation with leucine (Fig. 7G). These data strongly support the idea that leucine stimulation induces the activation of GDH, thereby enhancing the TCA cycle and ATP production in mitochondria, which results in Ca^{2+} influx in islets.

Correlation between $[ATP]_c$ and oscillating $[Ca^{2+}]_c$ in high-glucose conditions – It is well known in GSIS that $[Ca^{2+}]_c$, following its initial elevation, decreases and then starts to oscillate, which in turn induces oscillatory secretion of insulin (6). However, the mechanism underlying the $[Ca^{2+}]$ oscillation in GSIS remains controversial. One of the candidates is the oscillation of $[ATP]_c$. In an earlier study, oscillation of $[ATP]_c$ in pancreatic islets was implied by the observation that single islets expressing firefly luciferase, which requires ATP for light emission, showed oscillatory luminescence in both low- and high-glucose conditions (28). However, in our study, as well as in other recent studies (14, 15), oscillations were not observed in low glucose conditions. Because luminescence by firefly luciferase is susceptible to various factors, including oxygen, acetyl-CoA, and availability of luciferin, it is difficult to exclude the possibility that oscillatory luminescence in luciferase-expressing islets resulted from perturbation by the above factors. A recent study showed that mitochondrial energy metabolism does not oscillate in INS-1 832/13 insulinoma cells (29). However, it is still

possible that the oscillation of glycolysis drives $[ATP]_c$ in pancreatic β-cells. We compared the dynamics of $[ATP]_c$ with $[Ca^{2+}]_c$ in glucose-stimulated single islets. After stimulation with high glucose, $[ATP]_c$ increased sharply and then remained at high levels. In contrast, $[Ca^{2+}]_c$ started to oscillate following the first burst phase. We could not observe clear oscillatory behaviors in $[ATP]_c$ even when $[Ca^{2+}]_c$ was oscillating (Fig. 8A). At the dispersed single β-cell level, we always see that 25mM glucose caused a sustained rise in ATP levels with no clear oscillations over a period of 10 minutes (Fig. 2G); which is similar to what we observed in whole islets. Moreover, cross-correlation analyses for $[ATP]_c$ and $[Ca^{2+}]_c$ in individual glucose-stimulated islets did not reveal any correlation between $[ATP]_c$ and $[Ca^{2+}]_c$ dynamics during a period of Ca^{2+} oscillation (Fig. 8B). If the oscillation of $[ATP]_c$ occurred with the same frequency as that of $[Ca^{2+}]_c$, the frequency for $[ATP]_c$ should be typically less than 0.5/min. We have to note that GO-ATeam1 has enough dynamic sensitivity to detect oscillations of $[ATP]_c$, if they were to exist (17). The FRET signal of GO-ATeam1 was not saturated in islets undergoing $[Ca^{2+}]_c$ oscillations at 25 mM glucose because further increasing the glucose concentration to 42 mM resulted in a further elevation of the FRET signal (Fig. 8C). Next, in order to exclude the possibility that oscillation of $[ATP]_c$ is hindered by the non-physiological, abrupt increase in glucose (from 2.8 to 25 mM) in the above experiments, the glucose concentration in the medium was gradually increased in a stepwise manner. Whereas $[Ca^{2+}]_c$ began to oscillate at 11 mM glucose, $[ATP]_c$ gradually increased with increasing glucose concentration without significant oscillations (Fig. 8D).

Dynamics of $[ATP]_c$ and $[Ca^{2+}]_c$ upon arrest of energy metabolism – Whereas $[Ca^{2+}]_c$ oscillated in the second phase of GSIS, $[ATP]_c$ was sustained at high levels. We investigated whether sustained high $[ATP]_c$ is necessary for the oscillation of $[Ca^{2+}]_c$. Treatment of islets that were pretreated with high glucose, with CCCP, an uncoupler of mitochondrial membrane potential, resulted in the rapid cessation of $[Ca^{2+}]_c$ oscillation (Fig. 9A). Likewise, $[Ca^{2+}]_c$ oscillations also stopped immediately after the glucose concentration was lowered from 25 mM to 2.8 mM (Fig. 9B). In both cases, $[Ca^{2+}]_c$ oscillation stopped as soon as $[ATP]_c$ began to decrease. It is most likely that sustained high $[ATP]_c$ and/or high energy metabolism is required for islets to continue to exhibit $[Ca^{2+}]_c$ oscillations in GSIS.

Dynamics of $[ATP]_c$ and $[ATP]_m$ upon depletion of either extracellular or intracellular Ca^{2+} – Finally, we investigated the role of Ca^{2+} on glucose-induced intracellular ATP elevation. Ca^{2+} is known to enhance the activities of several mitochondrial dehydrogenases in the TCA cycle (30). Indeed, buffering of mitochondrial Ca^{2+} resulted in reduced insulin secretion in isolated rat islets (31). Several molecules have been implicated in Ca^{2+} transport to the mitochondria (32-35). Of these, a Ca^{2+}-sensitive mitochondrial uniporter called MCU is involved in mitochondrial Ca^{2+} homeostasis in pancreatic islets because its silencing impairs mitochondrial Ca^{2+} uptake in isolated islets (9). In the particular context of glucose stimulation, however, it has been unclear where the mitochondrial Ca^{2+} comes from. First, we investigated the role of extracellular Ca^{2+}. We depleted Ca^{2+} from the medium and monitored ATP levels. When the